Dyes and Pigments 213 (2023) 111179

Contents lists available at ScienceDirect

Dyes and Pigments

journal homepage: www.elsevier.com/locate/dyepig

Effect of bulky side groups on photophysical properties and electroluminescent performance of oligo(styryl)benzenes

Fernando de Lera-Garrido [a,b,1], Rocío Domínguez [a,b,1], M. Paz Fernández-Liencres [c], Cristina Martín [d], Juan Tolosa [a,b,**], Eva M. García-Frutos [e], Josefina Perles [f], Johan Hofkens [g], Joaquín C. García-Martínez [a,b], Andrés Garzón-Ruiz [d,*], Amparo Navarro [c,***]

[a] Departamento de Química Inorgánica, Orgánica y Bioquímica, Facultad de Farmacia, Universidad de Castilla-La Mancha, C/ José María Sánchez Ibañez s/n, 02071, Albacete, Spain
[b] Universidad de Castilla-La Mancha, Centro Regional de Investigaciones Biomédicas (CRIB), C/Almansa s/n, 02071, Albacete, Spain
[c] Departamento de Química Física y Analítica, Facultad de Ciencias Experimentales, Universidad de Jaén, Campus Las Lagunillas, 23071, Jaén, Spain
[d] Departamento de Química Física, Facultad de Farmacia, Universidad de Castilla-La Mancha, C/ José María Sánchez Ibáñez s/n, 02071, Albacete, Spain
[e] Instituto de Ciencia de Materiales de Madrid (ICMM), CSIC, Campus de Cantoblanco, 28049, Madrid, Spain
[f] Laboratorio de Rayos X de Monocristal, Servicio Interdepartamental de Investigación, Universidad Autónoma de Madrid (UAM), Cantoblanco, 28049, Madrid, Spain
[g] KU Leuven, Leuven Chem&Tech - Molecular Imaging and Photonics (MIP), Celestijnenlaan 200F Post Box 2404, 3001, Leuven, Belgium

ARTICLE INFO

Keywords:
Tris(styryl)benzene
tetra(styryl)benzene
Bulky side groups
Aggregation induced emission
Organic light-emitting devices

ABSTRACT

The rational design of electroluminescent compounds has been recognized as a promising strategy to maximize the efficiency of electronic devices. In this work, we analyze the impact of the substitution of *n*-alkyl and *n*-alkoxy side chains by bulkier side groups (*tert*-butyl and *tert*-butoxy) on the photophysics of the two model fluorophores 1,3,5-tris(styryl)benzene and 1,2,4,5-tetra(styryl)benzene. We found that the bulky side groups have a significant contribution to the vibrational normal modes associated with the non-radiative deactivation. The aggregation-induced enhanced emission phenomenon observed in some cases was attributed to the blocking of the *trans*→*cis* photoisomerization and the restriction of intramolecular vibrations. In the solid state, the bulky side groups have demonstrated to play a determining role in the supramolecular structure and photophysical properties, particularly in the case of the tetra(styryl)benzenes. In light-emitting devices, we found that the incorporation of the bulky side groups in oligo(styryl)benzenes could reduce the electromer formation and improve the device performance. The tetra(styryl)benzenes, and particularly the *tert*-butyl derivative, showed better device performance, with lower turn-on voltage, higher current density and electroluminescent intensity.

1. Introduction

The development of highly emissive fluorophores represents a vast field of research in which experimentalists and theoreticians print their effort in order to design new materials with singular applications from molecular electronics [1,2] to biosensing [3,4]. In general, the photophysical properties depend on the electron-donor or -withdrawing character of the substituents that bind to the π-conjugated backbone and these properties are hardly changed in solution if the side chains are elongated, or the peripheral groups are bulky. One of the main handicaps in this area is that many compounds quench their emission when molecules come into contact each other in powder, thin films, organogels, nanoparticles, etc. losing those desirable properties for which they were originally designed [5–8]. Intermolecular interactions have demonstrated to play a crucial role in the photophysical properties of many emissive compounds due to their direct impact into the arrangement of the molecules in aggregates and solid state [9]. Mechanochromism is a representative example of this in which intermolecular

* Corresponding author.
** Corresponding author. Departamento de Química Inorgánica, Orgánica y Bioquímica, Facultad de Farmacia, Universidad de Castilla-La Mancha, C/ José María Sánchez Ibañez s/n, 02071, Albacete, Spain.
*** Corresponding author.
E-mail addresses: juan.tolosa@uclm.es (J. Tolosa), andres.garzon@uclm.es (A. Garzón-Ruiz), anavarro@ujaen.es (A. Navarro).
[1] These authors have contributed equally to this work.

https://doi.org/10.1016/j.dyepig.2023.111179
Received 2 September 2022; Received in revised form 9 February 2023; Accepted 20 February 2023
Available online 23 February 2023

interactions can be altered applying external mechanical forces over an emissive compound which partly changes its packing mode and photophysical properties [10]. Furthermore, intermolecular contacts could be responsible for blocking intramolecular process such as photoisomerization and molecular vibrations and rotations which commonly have a strong impact over emissive properties [11]. Therefore, there is an engaged teamwork between inter- and intramolecular factors which determines the final photophysical properties of materials. A common strategy to preserve the intrinsic photophysical properties of the emitters in the solid state can be the introduction of bulky substituents to prevent the approximation between neighboring molecules and the undesirable π-π intermolecular interactions. These interactions have shown to be responsible for the decrease of emission upon aggregation in a large amount of fluorophores with the name of ACQ (aggregation-caused quenching) [12]. In this context, the length of linear alkyl chains attached to the peripheral phenyl rings has demonstrated to be very effective to tune the photophysical properties in a huge variety of emissive compounds [13] while the effect of branched alkyl chains has been less explored so far. [14] In the case of optoelectronic applications, the incorporation of branched or bulky substituents in the molecular structure of a fluorophore could also have a strong impact on the semiconductor performance of the device. A higher separation between neighboring molecules could lead to a weaker intermolecular electronic coupling and inefficient charge transport [15–17]. The understanding and controlling of the delicate balance between supramolecular organization and suitable photophysical and semiconducting properties is a really challenging task [18–20].

Different theories have been proposed to understand the photophysical response of organic materials to the light absorption considering a large variety of inter and intramolecular parameters. If the molecules are visualized as isolated entities in solution, the photophysics is mainly influenced by the solvent. However, if those molecules are part of aggregates in solution or even solid phases, the final emission properties depend mostly on the electronic interactions between fluorophore units. The classical theories by Kasha et al. [21–23] and more recently by Spano and Hestand [24,25] established a classification between *J* and *H* aggregates as a result of different long and short range excitonic couplings between neighboring chromophores which would modify their final electronic structure and emitting properties. Another widespread theory to explain changes in the emissive properties was proposed by Tang et al. according to which the restriction of intramolecular vibrations (RIV) and rotations (RIR) could be responsible for the enhancement of the radiative relaxation in a huge variety of π-conjugated compounds [26–28]. Trans→cis photoisomerization, restriction access to conical intersections (RACI) between the potential energy surfaces of the ground and excited states, intramolecular proton transfer (ESIPT) have also been successful interpretating the photophysical properties in different emissive compounds [29–31]. The thorough knowledge of the main mechanism responsible for the photophysics in different compounds has helped in the rational design of new fluorophores stablishing different strategies to achieve appropriate optoelectronic properties depending on the specific applications of the emissive compound.

Compounds in which double bonds and benzene rings combine to form a π-extended structure as oligo(styryl)benzenes, polymers as poly (*p*-phenylene vinylene) (PPV) or complex dendritic structures constitute a vast family of hydrocarbons widely studied due to their attractive electronic and photophysical properties [9,18–20,32]. Since the early work in 1990 over the electroluminescence of PPV [33], great efforts have been devoted to the structural modification in numerous fluorophores with the aim to suppress the effects responsible for the fluorescence quenching in the solid state as well as preserving suitable charge transport properties. To the best of our knowledge, the first work which revealed dramatic changes in the fluorescence quantum yield of an oligo(styryl)benzene from solution to solid state was published in 1996 by Oelkrug et al. [34] In the present study, the photophysical properties of tris(styryl)benzenes and tetra(styryl)benzenes have been explored incorporating for the first time *tert*-butyl and *tert*-butoxy as substituents in the peripheral phenyl rings (**3SB-^{t}Bu**, **3SB-^{t}BuO**, **4SB-^{t}BuO** and **4SB-^{t}BuO**; see Scheme 1) with the aim to scrutinize the impact of these bulky substituents on their photophysical properties upon aggregation. In previous works [18,19,32], we studied the photophysical properties of oligo(styryl)benzenes scaffolds with non-branched side chains (**3SB-CH_3**, **3SB-OC_6H_{13}**, **4SB-CH_3** and **4SB-OC_6H_{13}**; see Scheme 1) in solution and solid state although the absence of crystal structure prevented us to conclude about the packing of the molecules in solid state and intermolecular interactions present in it. In this work, we report for the first time the X-ray crystal structure of alkyl or alkoxy substituted tris(styryl)benzenes and tetra(styryl)benzenes which may help to understand the photophysical properties in solid state of these extensively studied compounds analyzing molecular packing and intermolecular interactions. Spectroscopic and electrochemical characterization, together with density functional theory (DFT) calculations have been addressed both in solution and solid state. The symbiosis between experimental and theoretical tools provides further understanding of the relationship between intermolecular interactions, molecular packing, and emission properties. In addition, light-emitting devices based on the studied compounds were fabricated to assess their suitability for optoelectronic applications. The optoelectronic performance of the different devices, combined with DFT calculations on diverse parameters related to semiconducting properties of the emitting material, allowed for a wider perspective on the technological applicability of oligo(styryl)benzenes decorated with *tert*-butyl and *tert*-butoxy side groups.

2. Experimental section

2.1. General

In air- and moisture-sensitive reactions, all glassware was flame-dried and cooled under argon. All reagents and solvents obtained from commercial sources were used as received, except for tetrahydrofuran (THF), which was freshly distilled over sodium/benzophenone ketyl under a positive pressure of dry argon. THF and acetonitrile (ACN) were used as CHROMASOLV quality in spectroscopic experiments. ^{1}H NMR and ^{13}C NMR spectra were acquired at room temperature on a Varian Inova-500 instrument. The NMR chemical shifts (δ) are given in ppm and are referenced to the residual protons of the deuterated solvent or carbon nuclei (^{1}H, δ = 7.27 ppm; ^{13}C, δ = 77.0 ppm). MALDI-TOF mass spectra were recorded in positive detection mode.

2.2. Synthesis

The synthesis of compounds **3SB-^{t}Bu**, **3SB-^{t}BuO**, **4SB-^{t}BuO** and **4SB-^{t}BuO** was performed according to Scheme 2. Phosphonates **A** and **B** were obtained by Arbuzov reaction of 1,3,5-tris(bromomethyl)benzene and 1,2,4,5-tetrakis(bromomethyl)benzene, respectively, with triethyl phosphite following a standard methodology. More detailed information is collected in Supporting Information.

2.3. Single crystal X-ray diffraction

The single crystals of **3SB-^{t}Bu**, **3SB-^{t}BuO**, **4SB-^{t}Bu** were obtained by slow evaporation method of acetone, (1:1) tetrahydrofurane:methanol and (1:1) acetone:dicloromethane, respectively. The single crystal of **4SB-^{t}BuO** was obtained by liquid-liquid diffusion method of (1:3) diclorometane:hexane. Single-crystal X-ray diffraction (SCXRD) measurements were collected in a Bruker Kappa Apex II diffractometer using graphite-monochromated molybdenum K_α radiation (λ = 0.71073 Å). A summary of some crystal and refinement data for measurements at room temperature of compounds **3SB-^{t}Bu**, **3SB-^{t}BuO**, **4SB-^{t}Bu**, y **4SB-^{t}BuO** can be found in Table S6. CCDC 2041137–2041140 contain the

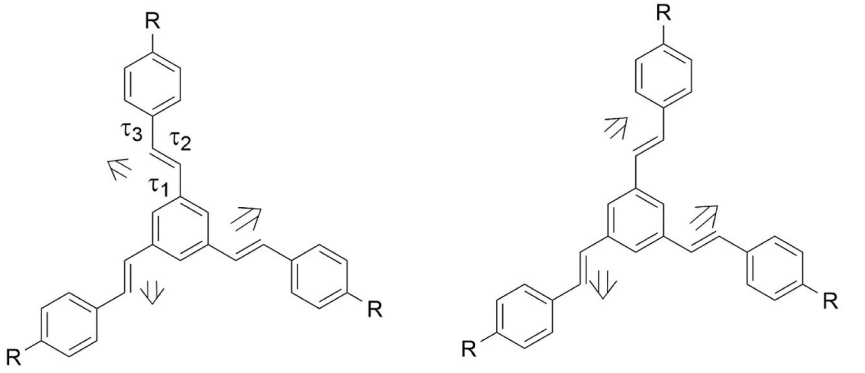

R = $-C(CH_3)_3$ **3SB-^{t}Bu**
R = $-OC(CH_3)_3$ **3SB-^{t}BuO**
R = $-CH_3$ **3SB-CH_3**
R = $-O(CH_2)_5CH_3$ **3SB-OC_6H_{13}**

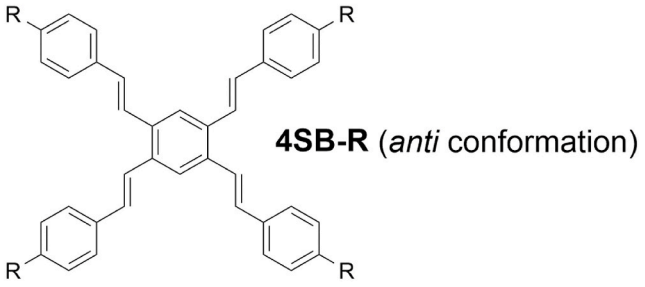

R = $-C(CH_3)_3$ **4SB-^{t}Bu**
R = $-OC(CH_3)_3$ **4SB-^{t}BuO**
R = $-CH_3$ **4SB-CH_3**
R = $-O(CH_2)_5CH_3$ **4SB-OC_6H_{13}**

Scheme 1. Chemical structures of the synthetized oligo(styryl)benzenes (**3SB-^{t}Bu**, **3SB-^{t}BuO**, **4SB-^{t}Bu** and **4SB-^{t}BuO**) as well as some reference oligo(styryl) benzenes (**3SB-CH_3**, **3SB-OC_6H_{13}**, **4SB-CH_3** and **4SB-OC_6H_{13}**). Only the full-trans configuration was considered in the spectroscopic and theoretical study of **3SB-R** and **4SB-R** compounds. The molecular structure and electronic properties of **3SB-R** derivatives were calculated for both the *sym* and *anti* rotamer. $\tau_{1\text{-}3}$ are three dihedral angles selected to describe the molecular structure of the studied compounds.

crystallographic data, that can be obtained free of charge from the Cambridge Crystallographic Data Centre *via* www.ccdc.cam.ac.uk/data_request/cif.

Diffraction measurements of the crystals of **3SB-^{t}Bu**, **3SB-^{t}BuO**, and **4SB-^{t}Bu** were made at low temperatures to improve the signal to noise ratio. In the case of compound **4SB-^{t}Bu**, the crystals were extremely unstable out of the mother liquor and suffered from loss of crystallinity even when covered in mounting oil and placed under nitrogen atmosphere. These three samples also display statistical disorder in many fragments: in **4SB-^{t}Bu**, carbon atoms C87-C92 are randomly located in two positions (A and B) with 51%–49% occupations, many of the methyl groups in the two molecules found in the asymmetric unit are heavily disordered, and only the most populated position (50%) could be located for C27-C30, C40-C42, C52-C54, C70-C72, C82-C84, C94-C96, C106-C108. Also, some partially disordered interstitial water molecules were found in the voids. In **3SB-^{t}BuO**, carbon atoms C17, C39-C42, C49-C56 and C81-C84 (and interstitial water oxygen O7W and O8W) were also heavily disordered, and only the position with the largest electron density (50%) could be located and isotropically refined, with the aid of geometrical restraints. **3SB-^{t}Bu** also displays disorder in the two molecules in the asymmetric unit: C7-C18 in one of them (with occupations 60% for position A and 40% for B) and C75-C84 in the other, with 56% and 44% for A and B respectively (except methyl carbons C82B, C83B and C84B where only 22% of the density could be located). Interstitial partially disordered water molecules were also included in the model.

2.4. Spectroscopy experiments

Sample concentration of 3 μM was employed for UV–Vis absorption and fluorescence measurements of the free molecule in solution. Solvent mixtures (ACN/water and THF/water) and sample concentrations of 5 μM were used for the molecular aggregation experiments. Quartz cuvettes (Hellma Analytics) of 10 mm were employed for all the absorption and fluorescence emission measurements in liquid samples. UV–Vis absorption spectra were acquired at 298 K on a V-750 spectrophotometer (JASCO) using a slit width of 0.4 nm and a scan rate of 600 nm min^{-1}. Steady-state fluorescence spectra were acquired in a FS5 spectrofluorometer (Edinburgh Instruments) equipped with a 150 W Xe lamp as the light source and a PMT (photomultiplier tube) detector (R928P model). Time-resolved fluorescence spectra were performed in a FLS920 (Edinburgh Instruments) spectrofluorometer equipped with a sub-nanosecond pulsed light-emitting diode, EPLED-360 (Edinburgh Photonics), a MCP-PMT (microchannel plate-photomultiplier tube) detector (R3809 model) and a TCSPC (time-correlated single photon counting)

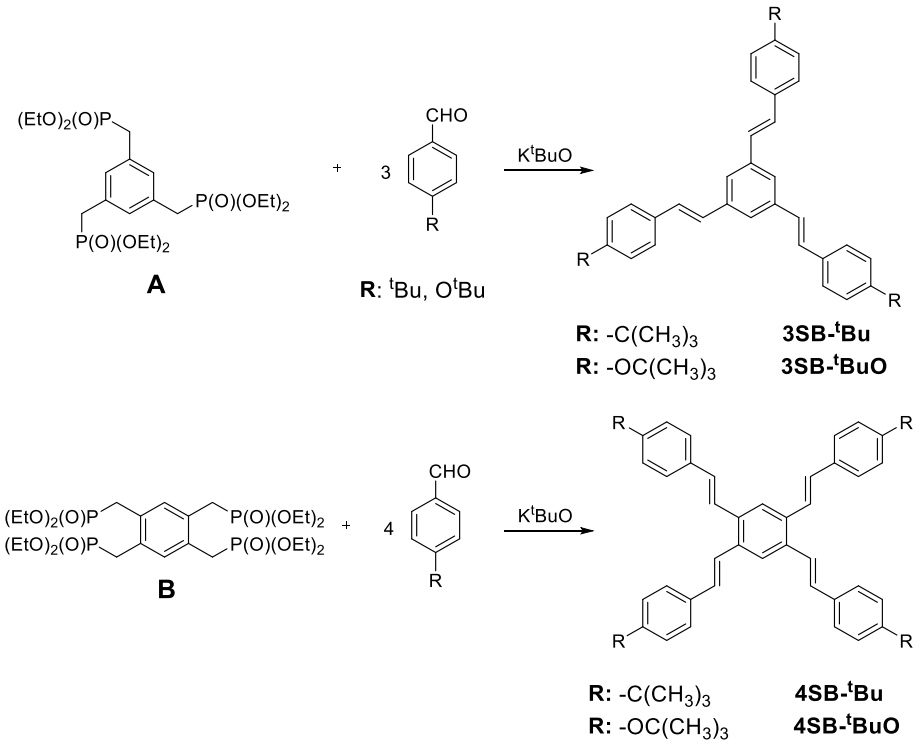

Scheme 2. Synthesis of **3SB-^{t}Bu**, **3SB-^{t}BuO**, **4SB-^{t}BuO** and **4SB-^{t}BuO**.

data acquisition card (TCC900 model). The fluorescence spectra and quantum yield of the solid samples were obtained using an integrating sphere coupled to the FS5 spectrofluorometer. The quantum yield of the liquid samples was also obtained using the integrating sphere. In solution, sample concentrations were $\leq$1 μM (and absorbance $\leq$0.1) for quantum yield measurements, excepting for the aggregation experiments (5 μM). In aggregation experiments, THF/water and acetonitrile/water mixtures were used as solvent and as reference. Quantum yield calculations were carried out using the F980 Software of Edinburgh Instruments.

2.5. Diffusion light-scattering (DLS) measurements

DLS measurements were recorded employing a Zetasizer NanoZS (Malvern Instruments). The studied compounds were solved in different THF/water mixtures. Solutions were not filtered.

2.6. Electrochemistry

Cyclic voltammetry (CV) and Osteryoung square wave voltammetry (OSWV) measurements were carried out in *o*-dichlorobenzene/acetonitrile 4:1 solutions. Tetrabutylammonium perchlorate (0.1 M as supporting electrolyte) was purchased from Acros and used without purification. Solutions were deoxygenated by argon bubbling prior to each experiment which was run under argon atmosphere. Experiments were done in a one-compartment cell equipped with a glassy carbon working electrode (ø = 2 mm), a platinum wire counter electrode, and an Ag/$AgNO_3$ (0.01 M in the supporting electrolyte) electrode as reference. Ferrocene/ferrocenium redox couple (Fc/Fc^+) was used as an internal reference in order to determine the oxidation potentials of the studied compounds. The data were transformed into frontier molecular orbital (FMO) energy levels *vs.* vacuum.

2.7. OLED fabrication

A single-layer device of each compound was fabricated using the following configuration: ITO anode/PEDOT:PSS (40 nm)/active compound (~50 nm, spin coated from 3 mg mL^{-1} in ACN solution)/Al cathode (150 nm)). An indium-tin-oxide (ITO)-coated glass (~109 Ω cm) was used as substrate. Before use, the glass was washed by immersion and sonication for 10 min in following solvents: 1) alkaline-detergent water (Hellmanex solution), water, acetone and isopropanol. The cleaned ITO-glasses were treated in an ultraviolet-ozone reactor (30 min) to lower the work function of the ITO layer. After that, a solution of the hole-injection layer, poly(3,4-ethylenedioxythiophene): polystyrene (PEDOT:PSS; Sigma Aldrich, high conductivity), was spin coated at 3000 rpm for 120 s and subsequently annealed at 150 °C during 15 min. Next, a 5 mg mL^{-1} solution of the selected carbazoles in acetonitrile (Sigma Aldrich, anhydrous), was spin coated for 60 s at 1000 rpm and annealed at 80 °C for 15 min. Finally, a 150 nm aluminum (Al) electrode layer was vapor deposited on top of the emissive layer. Stationary electroluminescence measurements were recorded using an Edinburgh FLS 980 fluorimeter where the Xe-lamp (usually for optical excitation) was blocked in order to only register the electroluminescence spectra. Current – Voltage (I–V) curves were measured in the dark at room temperature using a Keithley 2400 device.

2.8. Computational details

Full geometry optimizations of the ground (S_0) and first excited (S_1) states were performed using Gaussian 09 program package (version D.01) [35] at the M06-2X/6-31G** and B3LYP/6-31G** levels of theory [36]. M06-2X/6-31G** was chosen because it has shown suitable results in previous works of related oligo(styryl)benzenes and was the functional mainly used in the present work [7,18–20,32]. The vibrational frequencies were computed to check the absence of imaginary frequencies. The molecular geometries from X-ray diffraction were taken as starting point for the geometry optimization in the ground state and a conformational analysis was performed searching the most stable conformation in solution. Polarizable continuum model (PCM) was used to include the effect of the solvent as it has been as implemented in the Gaussian package [37–39]. For both **3SB-^{t}Bu** and **3SB-^{t}BuO** derivatives,

the *anti* configuration was predicted as the most stable in THF solution (see Scheme 1) being very close in energy to the *sym* configuration (see Fig. S33 and Table S9). According to that, both *anti* and *sym* have been considered in the photophysical analysis in solution. It should be pointed out that from the X-ray crystal structure, both *sym* and *anti* configuration were solved for **3SB-^{t}BuO** while only the *anti* configuration for **3SB-^{t}Bu**. For both **4SB-^{t}Bu** and **4SB-^{t}BuO** derivatives, a *pseudo*-C_i conformation that reminds of the 'frog-leap' was predicted as the most stable in solution, but this configuration only was found in the crystal structure of **4SB-^{t}BuO**. However, a *pseudo*-C_{2v} configuration resembling the free-fall of a paratrooper was solved from the X-ray crystal structure of **4SB-^{t}Bu**. In this case, according to the relative energies, only the *pseudo*-C_i configuration has been considered for the photophysical analysis in solution.

Vertical electronic transitions and geometry optimization of the excited electronic states were computed using Time-Dependent DFT calculations (TD-M06-2X/6-31G**) in solution. The fluorescence emission energy from the first excited state was calculated at the same level of theory as

$$E_{em}(S_1) = E_{S1}(G_{S1}) - E_{S0}(G_{S1}) \quad (1)$$

where $E_{S1}(G_{S1})$ is the energy of the S_1 state at its equilibrium geometry (G_{S1}), in the state-specific solvation approach [40]; and $E_{S0}(G_{S1})$ corresponds to the energy of the S_0 state at the S_1 state geometry (G_{S1}) and with the static solvation from the excited state [41].

The vibrational reorganization energy associated to the non-radiative relaxation of excited electronic states, λ, was computed using the program DUSHIN developed by Reimers [42] according to:

$$\lambda = \sum_i \lambda_i = \sum_i \hbar\omega_i S_i \quad (2)$$

where ω_i is the wavenumber associated to the vibrational mode *i*, which assist the internal conversion process, and S_i is the dimensionless Huang-Rhys (HR) factor calculated from the atomic displacements ΔQ and force constant, *k*, of the normal mode *i* according to [42]:

$$S_i = \frac{1}{2} k \frac{\Delta Q^2}{\hbar\omega_i} \quad (3)$$

The solid state was simulated using a two-layer ONIOM approach [43–46] building a model cluster from the X-ray crystallographic data. The central active molecule was treated with M06-2X/6-31G** and B3LYP/6-31G** (high level) and both S_0 and S_1 electronic state geometries were fully optimized. This central molecule was surrounded by several molecules (low level) treated by molecular mechanics (MM) using the UFF [47] force field with their molecular geometries frozen.

Different parameters related to the semiconducting properties were also computed for the studied compounds. Firstly, the charge-transfer rate constant (k_{CT}) was calculated in the context of the hopping model on the basis of the semi-classical Marcus theory according to the equation [48].

$$k_{CT} = \frac{4\pi^2}{h} \frac{1}{\sqrt{4\pi\lambda k_B T}} t^2 \exp\left(\frac{-\lambda}{4k_B T}\right) \quad (4)$$

where λ and t are the reorganization energy and the charge-transfer integral, respectively. The intermolecular charge transfer integral for hole (t_+) and electron (t_-) were computed for each charge transport pathway using couple of molecules extracted from the crystal structure and using of the so-called dimer projection approach implemented in the code *J-from-g03* [49,50]. Both λ and t were calculated at the B3LYP/6-31G** level of theory in gas phase. In this context, λ was calculated using the Nelsen's four-point approach. λ is the sum of two terms $\lambda = \lambda_1 + \lambda_2$ which corresponds to the geometry relaxation energies upon going from the neutral-state geometry to the charged-state one and *vice versa:*

$$\lambda_1 = E^0(G^*) - E^0(G^0) \quad (5)$$

$$\lambda_2 = E^*(G^0) - E^*(G^*) \quad (6)$$

where $E^0(G^0)$ and $E^*(G^*)$ are the ground-state energies of the neutral and ionic states, respectively. $E^0(G^*)$ is the energy of the neutral molecule at the optimal ionic geometry, and $E^*(G^0)$ is the energy of the charged state at the optimal geometry of the neutral molecule. Additionally, the adiabatic ionization potentials (AIP) and electron affinities (AEA) were calculated as follows for the cationic state

$$AIP = E_+(G_+) - E_0(G_0) \quad (7)$$

and for the anionic state

$$AEA = E_0(G_0) - E_-(G_-) \quad (8)$$

where $E_0(G_0)$, $E_+(G_+)$ and $E_-(G_-)$ are the ground-state energies of the neutral, cationic and anionic ionic states, respectively.

3. Results and discussion

3.1. Photophysical properties in solution

The synthesis of oligo(styryl)benzenes was carried out by the Horner-Wadsworth-Emmons reaction. This methodology allows a high control in the stereochemistry of the double bonds, obtaining exclusively the diastereoisomers in *trans* configuration for all of them, as can be observed in the value of $J = 16$ Hz for the coupling constants of the olefinic protons in the ^{1}H NMR spectra (see Supporting Information). The absorption and fluorescence emission spectra of the synthetized compounds were recorded in different solvents (see Fig. 1(a) and S7). We found a good match between the recorded absorption maxima (λ_{ab}^{max}) and the corresponding vertical transition wavelengths (λ_{vert}^{max}) computed at the TD-M06-2X/6-31G** level of theory (see Tables 1 and S10). The solvent polarity and the presence of the oxygen atom in the side group (*tert*-butoxy *vs. tert*-butyl) have a minor effect on their absorption spectra. No significant differences between the absorption spectra of the studied compounds and those reported for their methyl, methoxy and *n*-hexyloxy derivatives were also found [19,32]. The absorption maxima of the tetra(styryl)benzene derivatives are red-shifted ($\Delta\lambda_{ab}^{max} \geq 20$ nm in THF) with respect to the tris(styryl)benzene derivatives. This agrees with the fact that *ortho* and *para* substitution leads to more effective conjugation than *meta* substitution which leads to the consequent reduction of the optical band gap. The lowest-energy absorption band of tris(styryl)benzene derivatives, with a *pseudo*-C_3 symmetry (*sym* configuration; Fig. S33), was assigned to two electronic transitions ($S_0 \rightarrow S_1$ and $S_0 \rightarrow S_3$) involving diverse degenerate molecular orbitals (see Fig. S34). Accordingly, close wavelengths were calculated for $S_0 \rightarrow S_1$ and $S_0 \rightarrow S_3$ transitions of *sym*-**3SB-^{t}BuO** ($\lambda_{vert}^{calc} = 304$ and 302 nm, respectively) and a similar behavior was found for *sym*-**3SB-^{t}Bu**. HOMO-1, HOMO, LUMO and LUMO+1 frontier orbitals calculated for these molecules have V-shape and are located on two branches of the molecule. Curiously, a loss of orbital degeneracy was observed for the *anti* configuration of both molecules. For instance, higher differences were found between the wavelengths calculated for the three lowest-energy vertical transitions of *anti*-**3SB-^{t}BuO** ($\lambda_{vert}^{calc} = 311$, 303 and 294 nm for $S_0 \rightarrow S_1$, $S_0 \rightarrow S_2$ and $S_0 \rightarrow S_3$, respectively) and a similar behavior was observed for *anti*-**3SB-^{t}Bu**. As reported for 1,3-bis(styryl)benzene [51], both *sym* and *anti* conformations appear in the crystal structure of **3SB-^{t}BuO** (*vide infra*) being the *anti* rotamer slightly more stable than the *sym* one in THF solution ($\Delta E = 0.02$ kcal mol^{-1}; see Table S9 for details). The coexistence of both conformations and the thermal population of low-frequency torsional modes lead to a high spectral complexity and loss of the fine structure of the absorption band. Accordingly, a blue-shift is observed in the absorption spectra of both **3SB-^{t}BuO** and **3SB-^{t}Bu** upon temperature increases (Fig. 1(b) and S8). This fact can be related to a population enhancement of the *sym* rotamer.

The coexistence of different conformers also leads to the absorption and excitation spectra do not completely overlap (Fig. 1(c)) indicating that the *anti* rotamer has greater contribution to the fluorescence signal at room temperature.

The frontier orbitals calculated for tetra(styryl)benzene derivatives have X-shape and are significantly less degenerated than for the *sym*-tris (styryl)benzene derivatives (Fig. S34). For instance, a difference of 30 nm was computed between $S_0 \rightarrow S_1$ and $S_0 \rightarrow S_2$ transitions of **4SB-^{t}BuO** (with *pseudo*-C_i symmetry; see Table S10). Accordingly, the prominent shoulder observed at ~375 nm for **4SB-^{t}BuO** in THF solution could be associated to the $S_0 \rightarrow S_1$ transition (see Fig. 1(a)). Nevertheless, the coexistence of different conformers cannot be ruled out because the absorption spectrum is sensitive at the temperature and absorption and excitation fluorescence spectra do not completely overlap, as previously discussed in the case of tris(styryl)benzene derivatives (Figs. S8 and S9). Similar conclusions can be drawn for **4SB-^{t}Bu**. Interestingly, frontier-orbital degeneracy was also not found for 1,3-bis(styryl)benzene [52, 53]. The lowest energy absorption band of the derivative with two styryl branches was assigned to the $S_0(1^1A_g) \rightarrow S_1(1^1B_u)$ electronic transition which mainly involves HOMO and LUMO orbitals [52,53]. Thus, the number of styryl branches as well as the structural conformation play a critical role on the electronic properties of oligo(styryl)benzenes in solution while the nature, size and form of the of side chains seem to have a lesser impact. This conclusion is directly related to the fact that the π-conjugation and molecular orbitals involved in the electronic transitions are localized in the central skeleton and do not extend to the peripheral side chains.

All the studied compounds showed blue fluorescence emission in solution (Fig. 1(a), S7 and S16; Tables 1 and S3). Differences ≤0.25 eV between the emission maximum energies (λ_{em}^{max}) in THF solution and the calculated energies for the $S_1 \rightarrow S_0$ transitions ($\lambda_{S1 \rightarrow S0}^{calc}$) at the TD-M06-2X/6-31G** level of theory were found (see Table S11). Similar matches between experimental and theoretical energies were reported for the *n*-alkoxy derivatives **3SB-OC_6H_{13}** and **4SB-OC_6H_{13}** [19]. The fluorescence emission maxima of the tetra(styryl)benzene derivatives are significantly red-shifted ($\Delta\lambda_{em}^{max}$ > 60 nm in THF) with respect to their tris(styryl)benzene counterparts. The fluorescence spectra show fine structure, particularly for the tris(styryl)benzene derivatives in THF solution (Fig. 1(a) andS7). As discussed in a previous work, the vibronic coupling is probably due to the molecular planarization upon excitation of the tris(styryl)benzene core [19]. This planarization mainly involves a single styryl branch of the molecule (in the excitation of tetra(styryl) benzenes, the planarization involves two styryl branches; see Fig. S37, as well as Table S13). In addition, the higher energy difference between *sym* and *anti* conformers in the S_1 state (ΔE = 0.60 kcal mol^{-1} for **3SB-^{t}BuO**) than in the S_0 state, could increase the population of the most stable conformer (*anti*) (Table S9). This conformer could not only be the most abundant but also more fluorescent than the *sym* one, being the emission spectrum mainly attributable to the *anti* conformation. In this sense, the lower trans→cis energy barrier calculated for *sym*-**3SB-^{t}BuO** in the S_1 state suggests than the *sym* conformer is more sensitive to the trans→cis photoisomerization than *anti*-**3SB-^{t}BuO** (see Fig. 1(d)). It is well-known than trans→cis photoisomerization is one of the main non-radiative deactivation pathways of styryl-benzenes [53–56].

In addition, six normal modes with significant Huang–Rhys (HR) factors, associated with the internal conversion (IC) deactivation mechanism, were computed for *sym*-**3SB-^{t}BuO** (marked with a dotted circle in Fig. 2; see also Fig. S39 and Table S14). On the contrary, only two normal modes with large HR factors were computed for *anti*-**3SB-^{t}BuO**. Considering both the trans→cis photoisomerization and the IC deactivation, higher non-radiative constants might be expected for *sym*-**3SB-^{t}BuO** than for *anti*-**3SB-^{t}BuO**. Similar conclusions can be drawn from the HR factors and trans→cis energy barriers calculated for the *sym* and *anti* rotamers of **3SB-^{t}Bu**. Table 1 shows the fluorescence quantum yield recorded in different solvents. Considering THF as reference solvent, we observed that the quantum yields of the *tert*-butyl and *tert*-butoxy derivatives are somewhat smaller than those reported for their *n*-alkoxy homologues (34 and 36% for **3SB-^{t}Bu** and **3SB-^{t}BuO**, respectively; 41 and 47% for **4SB-^{t}Bu** and **4SB-^{t}BuO**, respectively; 60 and 57% for **3SB-OC_6H_{13}** and **4SB-OC_6H_{13}**, respectively) [19]. The important contribution of the *tert*-butyl and *tert*-butoxy groups to the normal modes associated with large HR factors (also calculated in THF solution) could be the cause of this difference (see Fig. S39). Nevertheless, some exceptions to this trend were also observed in more polar solvents (in DCM, Φ_F = 43 and 40% for **3SB-^{t}BuO** and **3SB-OC_6H_{13}**, respectively; in ACN, Φ_F = 47 and 27% for **4SB-^{t}BuO** and **4SB-OC_6H_{13}**, respectively) [19], preventing general conclusions on the effect of the presence of bulky side chains on non-radiative deactivation channels of oligo(styryl)

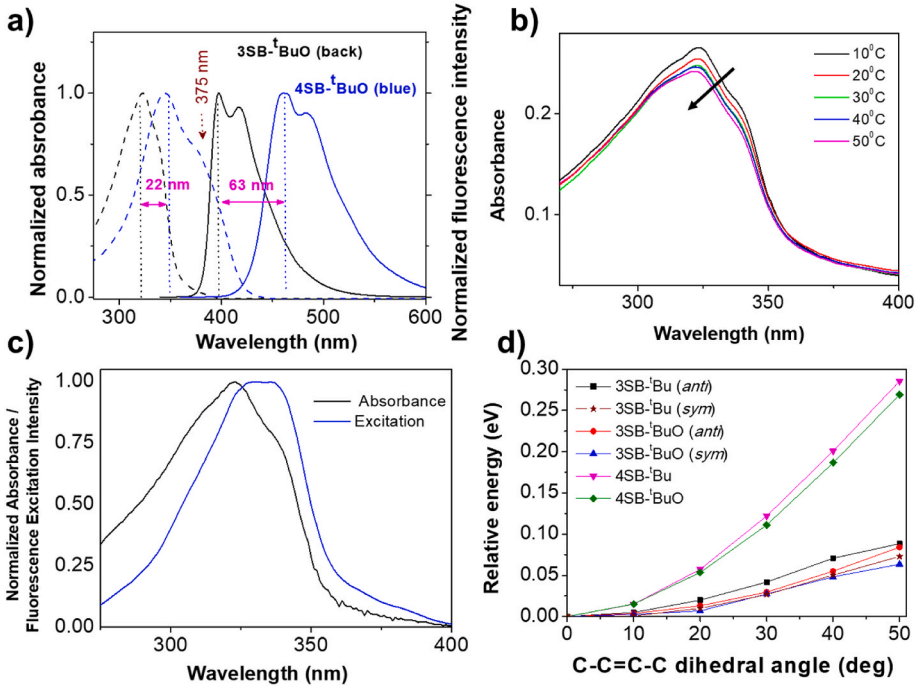

Fig. 1. (a) Absorption and emission fluorescence spectra of **3SB-^{t}BuO** and **4SB-^{t}BuO** recorded in THF solution (sample concentration was 3 μM). (b) Absorption spectrum of **3SB-^{t}BuO** recorded in THF solution at different temperatures. (c) Absorption and excitation fluorescence spectra of **3SB-^{t}BuO** recorded in THF. (d) Torsional barriers around the vinylene moiety in the S_1 excited state computed for **3SB-^{t}Bu** (*anti* and *sym*), **3SB-^{t}BuO** (*anti* and *sym*), **4SB-^{t}Bu** (*pseudo*-C_i) and 4SB-^{t}BuO (*pseudo*-C_i) at the M06-2X/6-31G** level of theory in THF solution. The zero level of energy corresponds to the full-trans configuration.

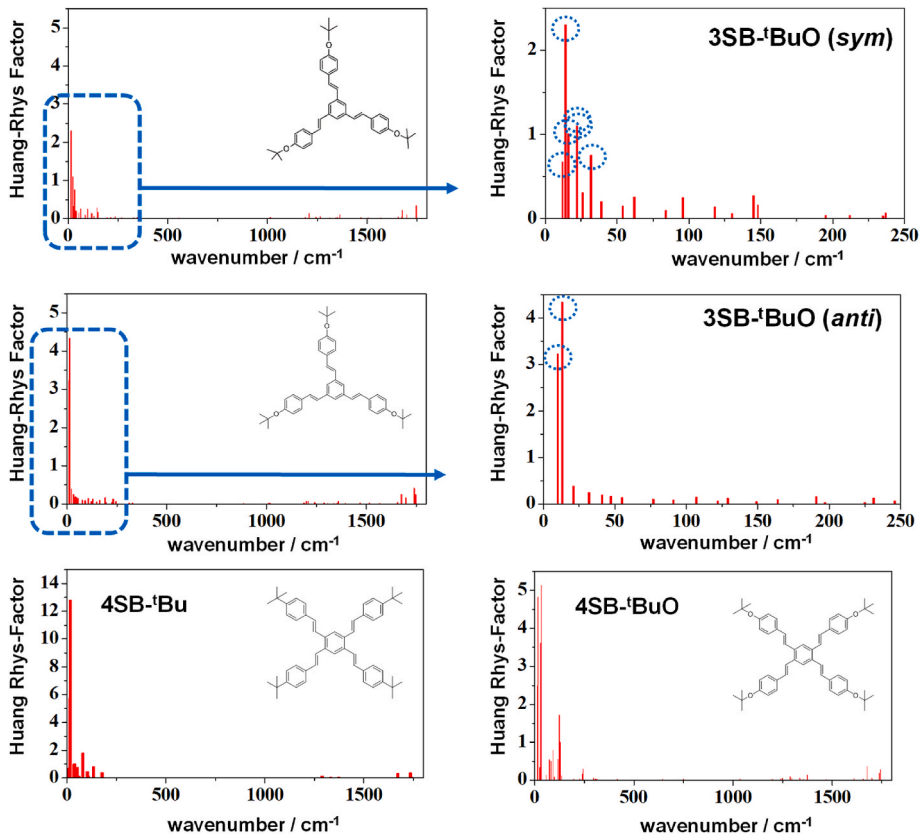

Fig. 2. Huang-Rhys factors *vs.* normal mode wavenumbers (in cm^{-1}) calculated for **3SB-^{t}BuO** (*sym* and *anti*), **4SB-^{t}Bu** and **4SB-^{t}BuO** in THF solution at the M06-2X/6-31G** level of theory. The dotted blue circles compare the most significant Huang-Rhys factors found for the *sym* and *anti* conformers of **3SB-^{t}BuO**.

Table 1
Absorption maximum wavelength (λ_{ab}^{max}), molar absorption coefficient (ε), fluorescence emission maximum wavelength (λ_{em}^{max}) and fluorescence quantum yield (Φ_F) determined in different solvents.

Compound	solvent	λ_{ab}^{max} (nm [eV])	ε (mM^{-1} cm^{-1})	λ_{em}^{max} (nm [eV])	Φ_F[a] (%)
3SB-^{t}Bu [b]	THF	320 [3.87]	84	393 [3.15] 415 [2.99]	34
	DCM	320 [3.87]	83	395 [3.14] 416 [2.98]	37
	ACN	318 [3.90]	93	393 [3.15] 413 [3.00]	26
3SB-^{t}BuO [c]	THF	323 [3.84]	86	397 [3.12] 417 [2.97]	36
	DCM	324 [3.83]	101	402 [3.08] 418 [2.97]	43
	ACN	321 [3.86]	103	418 [2.97]	29
4SB-^{t}Bu [d]	THF	340 [3.65]	75	455 [2.72] 478 [2.59]	41
	DCM	340 [3.65]	105	458 [2.71] 480 [2.58]	36
	ACN	339 [3.66]	76	454 [2.73] 478 [2.59]	39
4SB-^{t}BuO [e]	THF	345 [3.59]	88	460 [2.69] 483 [2.57]	47
	DCM	344 [3.60]	89	466 [2.66] 484 [2.56]	29
	ACN	344 [3.60]	117	466 [2.66] 484 [2.56]	33

[a] Determined by using an integration sphere at room temperature. The concentration of the samples was ≤1.0 μM and the absorbance ≤0.1.
[b] The excitation wavelength was 318 nm.
[c] The excitation wavelength was 320 nm.
[d] The excitation wavelength was 340 nm.
[e] The excitation wavelength was 343 nm.

benzenes. In general, it can be stated that the substitution of *n*-alkoxy chains by *tert*-butyl or *tert*-butoxy groups does not have a significant effect on the position of the emission maximum and only a moderate effect on the fluorescence quantum yield of oligo(styryl)benzenes in solution.

Aggregation-induced enhanced emission (AIEE) was found for the studied tris(styryl)benzene derivates (see Fig. 3, S12 and S14). In THF/water mixtures, the fluorescence quantum yield reached a maximum value of 58% for **3SB-^{t}Bu** ($f_w = 50\%$) and 64% for **3SB-^{t}BuO** ($f_w = 60\%$) (f_w is the fraction of water of the solvent mixture; see Table S1). At low water fractions (≤50%), where AIEE phenomenon is normally observed for tris(styryl)benzenes [18,19], the absorption bands of **3SB-^{t}Bu** and **3SB-^{t}BuO** did not show significant shifts suggesting a weak electronic coupling at the aggregate level (Fig. S10). An analogous photophysical behavior was reported for **3SB-OC$_6$H$_{13}$** in THF/water mixtures and it was attributed to the formation of slipped-stacking aggregates [19]. Although these aggregates were weakly coupled, the presence of nearby molecules could hinder the trans→*cis*-photoisomerization and restrict the molecular vibrations associated with the IC process (RIV mechanism) [19]. As mentioned, two significant HR factor values involved in the non-radiative IC decay were calculated for *anti*-**3SB-^{t}BuO** in THF solution (S_i = 3.2 and 4.3). These HR factors are associated with vibrational modes in the low energy region of 10 and 13 cm^{-1} that imply twisting motions of one or more styryl moieties with a remarkable contribution of their *tert*-butoxy groups (Fig. 2 and S39; Table S14). The most relevant HR factors found for *anti*-**3SB-^{t}Bu** (S_i = 1.1, 0.8 and 0.6) are also associated with twisting motions of one or more styryl moieties involving their *tert*-butyl groups (29, 60 and 13 cm^{-1}, respectively). The significant contribution of the *tert*-butyl and *tert*-butoxy side groups to those normal modes contrast with the case of **3SB-OCH$_3$**, where the methoxy groups have a less relevant contribution to the normal modes with the highest HR factors [19]. These observations were also

corroborated for the tetra(styryl)benzene derivates as discussed below. The average fluorescence lifetime of **3SB-^{t}BuO** exhibited an increase from about 10 ns in THF solution to 13 ns in THF/water mixtures with f_w = 30 and 50% (see Fig. S17 and Table S2). In these cases, DLS measurements showed the presence of small nanoparticles, with a Z-average radius between 1 and 2 nm (and high polydispersity, PdI) (see Fig. S20 and Table S5). On the contrary, the fluorescence emission was strongly quenched and significant changes were recorded in the absorption spectra of both **3SB-^{t}Bu** and **3SB-^{t}BuO** at high water fractions (≥60%). These results suggested that the molecules in the aggregate were more strongly coupled due to the increase of the solvent polarity. In THF/water mixtures with f_w = 80, large aggregates with a radius of about 400 nm for **3SB-^{t}Bu** (PdI ≤0.4) and 70 nm for **3SB-^{t}BuO** (PdI ≤0.2) were detected by DLS. Interestingly, the average fluorescence lifetime of **3SB-^{t}BuO** found in THF/water mixtures with f_w = 80 dropped up to 4 ns. In these conditions, a shorter fluorescence lifetime and, at same time, a smaller fluorescence quantum yield indicate a strong increase of the non-radiative rate constant in the aggregate as well as an increase of the radiative rate constant, but in lesser extent. In acetonitrile/water mixtures, maximum quantum yields of 60 and 48% were found for **3SB-^{t}BuO** (f_w = 60%) and **3SB-^{t}Bu** (f_w = 40%), respectively. The photophysical behavior in these mixtures was more complex than in THF/water mixtures because of the diverse shifts observed in the absorption spectra. In this case, an excitonic coupling between the molecules in the aggregate could be produced despite the presence of the bulky side groups. A thorough study on the Coulombic excitonic coupling in π-π stacking-aggregates of the model molecule **3SB-OC$_6$H$_{13}$** in acetonitrile/water mixtures can be consulted in the reference. [18] Interestingly, a strong decrease of both the fluorescence lifetime and quantum yield was also reported for **3SB-OC$_6$H$_{13}$** in acetonitrile/water mixtures with f_w = 80 with respect to the molecule solved in acetonitrile [18].

Small aggregates with a radius ≤2 nm were also detected for the studied tetra(styryl)benzenes THF/water mixtures with f_w = 30 and 50%. As observed for tris(styryl)benzenes, the size of the aggregate strongly increases for f_w = 80%, in parallel to a drop in the fluorescence lifetime (Figs. S17 and S20; Tables S2 and S5). AIEE was observed for the tetrabranched derivatives but the intensity of this phenomenon was clearly weaker than for their tris(styryl)benzene homologues (Fig. 3, S13 and S15). In THF/water mixtures, the fluorescence quantum yield reached a maximum value of 57% for **4SB-^{t}Bu** (f_w = 30%) and 59% for **4SB-^{t}BuO** (f_w = 30%). Curiously, the AIEE phenomenon was not observed for the *n*-alkoxy derivative **4SB-OC$_6$H$_{13}$**, neither in THF/water mixtures nor in ACN/water mixtures [19]. In that work, DFT calculations predicted that the columnar aggregates of **4SB-OC$_6$H$_{13}$** are more weakly coupled (with larger distances between the parallel planes of two neighboring molecules) than the columnar aggregates of **3SB-OC$_6$H$_{13}$** [19]. The intermolecular interactions of molecular aggregates of **4SB-^{t}Bu** and **4SB-^{t}BuO** should not be stronger than the aggregates of **4SB-OC$_6$H$_{13}$** because of their more bulky side chains. Accordingly, no significant shifts were observed in the absorption spectra of **4SB-^{t}Bu** and **4SB-^{t}BuO** upon aggregation at low water fractions (≤50%), as in the case of **4SB-OC$_6$H$_{13}$** [19]. Therefore, the origin of the AIEE phenomenon observed for both **4SB-^{t}Bu** and **4SB-^{t}BuO** does not seem to be associated to excitonic interactions.

The trans→cis isomerization barriers calculated for the tetra(styryl) benzene derivatives in the excited state are significantly higher than those calculated for the tris(styryl)benzenes and, consequently, the photoisomerization could have a smaller contribution to the non-radiative deactivation of the tetrabranched fluorophores (see Fig. 1 (b)). Concerning to RIV mechanism, we found that the vibrational frequencies with the highest HR values calculated for the tetra(styryl) benzene derivatives imply twisting motions of several styryl moieties with a significant contribution of their *tert*-butyl and *tert*-butoxy side chains (ω_i = 14 and 17 cm^{-1}; S_i = 5.8 and 12.8, respectively, for **4SB-^{t}Bu**; ω_i = 15 and 33 cm^{-1}; S_i = 4.8 and 5.1, respectively, for **4SB-^{t}BuO**; see Fig. 2 and S39, and Table S14). On the contrary, the vibrational modes with the high HR values calculated for **4SB-OCH$_3$** correspond to simultaneous phenyl wagging and hydrogen rocking causing a deformation of the entire molecule during vibration (note that similar findings were discussed above for the tris(styryl)benzene derivatives) [19]. The important contribution of the *tert*-butyl and *tert*-butoxy groups to the non-radiative deactivation of **4SB-^{t}Bu** and **4SB-^{t}BuO** could be involved in the AIEE phenomenon observed for these molecules and not for their *n*-alkoxy derivative, considering as hypothesis that the vibrations of bulky side groups would be more efficiently blocked upon aggregation than vibrations involving the whole molecule.

3.2. Photophysical properties in the solid state

The studied tris(styryl)benzene and tetra(styryl)benzene derivatives showed blue and green emission, respectively, in the solid state (see Fig. 4(b) and Table S3). Their fluorescence excitation and emission spectra are pointed out in Fig. 4(a) and S18. Table 2 collects the excitation and emission maximum wavelengths (λ_{ex}^{max} and λ_{em}^{max}) as well as the quantum yields recorded in different sample forms, i.e. powder, thin film and crystal. Interestingly, the fluorescence quantum yields were higher for the more amorphous samples (powder and thin films) than for their crystals. The largest quantum yields were determined for **3SB-^{t}BuO** (25–26% in powder and thin film) and for **4SB-^{t}Bu** (25% in thin film). On the contrary, markedly different quantum yields were reported for their *n*-alkoxy derivatives, i.e. **3SB-OC$_6$H$_{13}$** (50% in powder and 29–51% in thin film) [18] and for **4SB-OC$_6$H$_{13}$** (2% in powder) [19]. This results suggest that *n*-alkoxy chains have a smaller influence on the supramolecular structure than the nature of the conjugated core. Thus, the larger conjugated core of **4SB-OC$_6$H$_{13}$** favors π-stacking interactions, approximating molecules in the supramolecular structure, with dramatic effects on the luminescence emission properties [19]. It seems that *tert*-butyl and *tert*-butoxy groups play a more determining role in the control of the supramolecular structure and intermolecular molecular interactions of the studied fluorophores than *n*-alkoxy chains. The presence of the bulkier groups leads to a more balanced fluorescence quantum yields between tris(styryl)benzenes and tetra(styryl)benzenes. Crystals were obtained for all the studied compounds and their structures solved by single crystal X-ray diffraction. These crystal structures along with DFT calculations have allowed us to analyze the influence of the intermolecular interactions on the photophysical properties. ONIOM calculations were performed defining a cluster with enough molecules extracted from the experimental X-ray crystal to mimic the crystalline environment. In these clusters, both the ground state and excited state of a central active molecule was optimized while the surrounding ones are kept frozen (see Fig. 5). The central active molecule was treated with and both S_0 and S_1 electronic state geometries were fully optimized (high level with DFT). This central molecule was surrounded by several molecules (low level with UFF). The most relevant vertical absorption transitions were calculated for the active molecules of these clusters are collected in Tables 2 and S12. Additionally, the wavelengths calculated for the transition $S_1 \rightarrow S_0$ ($\lambda_{S1\rightarrow S0}^{calc}$), along with the experimental emission maxima, are shown in Table 2. Large differences between (excitation and emission) fluorescence maxima and wavelengths calculated for the ($S_0 \rightarrow S_1$ and $S_1 \rightarrow S_0$) electronic transitions with TD-M06-2X/6-31G** were found despite this method proved to be accurate in the calculation of the electronic transitions of the studied compounds in THF solution. This could evidence that the methodology used is insufficient to predict the photophysical properties of the crystal probably due to the treatment of electrostatic interactions between DFT and UFF layers. Interestingly, TD-B3LYP/6-31G** significantly improved the results obtained with TD-M06-2X/6-31G**. For instance, the differences between $\lambda_{S1\rightarrow S0}^{calc}$ and λ_{em}^{max} were in the range of 0.02–0.12 eV and 0.06–0.12 eV for the tris(styryl)benzene the tetra(styryl)benzene derivatives, respectively. This result could be due to the fact that B3LYP tends to

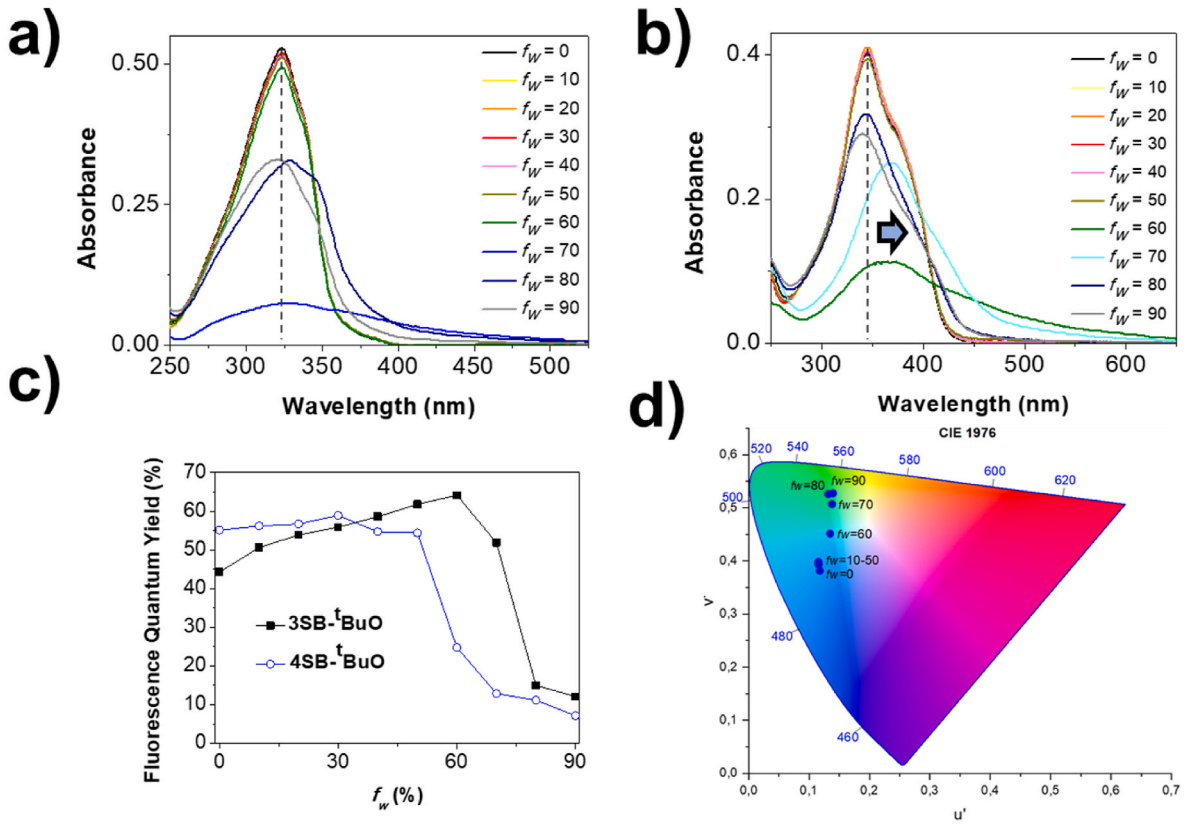

Fig. 3. Evolution of the absorption spectrum of (a) **3SB-^{t}BuO** and (b) **4SB-^{t}BuO** in different THF/water mixtures. (c) Evolution of the fluorescence quantum yields of **3SB-^{t}BuO** and **4SB-^{t}BuO** in different THF/water mixtures. (d) CIE 1976 diagram for **4SB-^{t}BuO** in different THF/water mixtures (the points 1 and 10 correspond to f_w = 0 and 90%, respectively). The sample concentration was 5.0 μM for the molecular aggregation experiments.

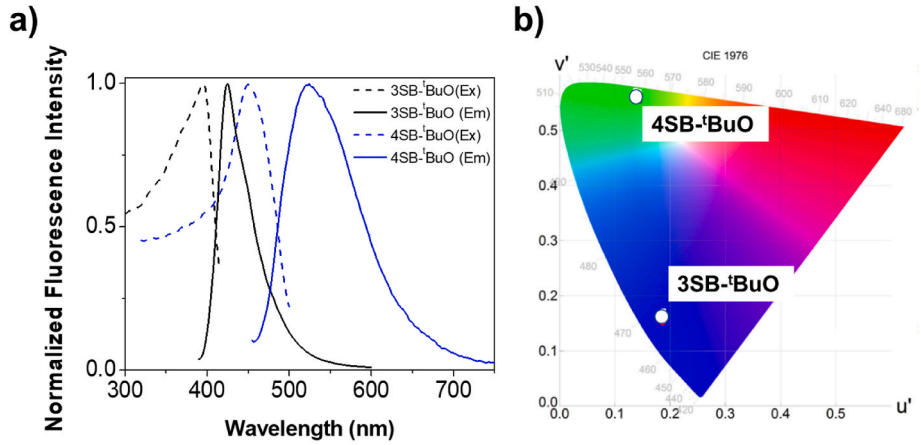

Fig. 4. (a) Fluorescence excitation and emission spectra of **3SB-^{t}BuO** and **4SB-^{t}BuO** in the solid state (powder). (b) Chromaticity diagram (CIE 1976) of **3SB-^{t}BuO** and **4SB-^{t}BuO** in the solid state (powder).

overestimate the electronic delocalization favoring more planar structures. According to Fig. S38, the optimization of the central molecule with B3LYP produces in general smaller τ_1 and τ_2 dihedral angles than M06-2X, and therefore closer values to the crystal structure.

Digging deeper into the crystal structures we found that the tris (styryl)benzene derivatives display two molecules in the asymmetric unit of the crystal (Figs. S23, S24 and S27). Both molecules (types 1 and 2) adopt *anti* conformation in the case of **3SB-^{t}Bu** and pack in columns with weak π-π and C-H···π intramolecular interactions (Fig. S28). This packing is the least dense among the structures here presented, leaving large channels where highly disordered solvent molecules are lodged. In the asymmetric unit of the crystal of **3SB-^{t}BuO**, there is a molecule in *sym* conformation and other in *anti* conformation. *anti*-**3SB-^{t}BuO** packs in columns and presents two of the arms almost coplanar with the central ring while the other one displays a much larger angle (53°) due to the C-H···π intramolecular contacts (see Fig. S29). *Sym*-**3SB-^{t}BuO** also packs in columns with weak π-π intramolecular interactions and shows a slight concave curvature with angles ≤23° between the outer and central rings. The quenching of the emission in solid state has been typically associated to π-π intermolecular interactions [57,58]. On the other hand, it has been reported that C-H···π intramolecular interactions restrict the molecular motions of bis(α-phenylstyryl)-benzene derivatives

Table 2
Fluorescence excitation and emission maxima (λ_{ex}^{max} and λ_{em}^{max}) determined in the solid state. Absorption and fluorescence emission wavelength calculated for the $S_0 \rightarrow S_1$ transition ($\lambda_{S0\rightarrow S1}^{calc}$) and $S_1 \rightarrow S_0$ transition ($\lambda_{S1\rightarrow S0}^{calc}$) in the solid state at the TD-M06-2X/6-31G** and TD-B3LYP/6-31G** levels of theory.

		Experimental			TD-B3LYP/6-31G**		TD-M06-2X/6-31G**	
Compd	Sample form	λ_{ex}^{max} (nm [eV])	λ_{em}^{max} (nm [eV])	Φ_F (%)	$\lambda_{S0\rightarrow S1}^{calc}$ (nm [eV])	$\lambda_{S1\rightarrow S0}^{calc}$ (nm [eV])	$\lambda_{S0\rightarrow S1}^{calc}$ (nm [eV])	$\lambda_{S1\rightarrow S0}^{calc}$ (nm [eV])
3SB-^{t}Bu	powder	394 [3.15]	421 [2.95]	13[e]				
	thin film	394 [3.15]	421 [2.95]	15[f]				
	Crystal	400 [3.10]	425 [2.92]	1[f]	381 [3.26][a]	422 [2.94][a]	303[4.09][a]	349 [3.56][a]
3SB-^{t}BuO	powder	395 [3.14]	424 [2.92]	25[e]				
	thin film	395 [3.14]	424 [2.92]	26[f]				
	Crystal	404 [3.07]	433 [2.86]	14[f]	376 [3.30][a]/381 [3.25][b]	420 [2.96][a]/422 [2.94][b]	309[4.01][a]/297 [4.17][b]	354 [3.51][a]/356 [3.49][b]
4SB-^{t}Bu	powder	456 [2.72]	518 [2.39]	13[g]				
	thin film	456 [2.72]	518 [2.39]	25[h]				
	Crystal	440 [2.82]	502 [2.47]	20[i]	415 [2.99][c]	480 [2.59][c]	332[3.74][c]	408 [3.04][c]
4SB-^{t}BuO	powder	449 [2.76]	524 [2.37]	5[j]				
	thin film	449 [2.76]	524 [2.37]	12[k]				
	Crystal	466 [2.66]	516 [2.40]	3[l]	430 [2.88][d]	505 [2.46][d]	344[3.60][d]	419 [2.96][d]

[a] *anti* conformation.
[b] *sym* conformation.
[c] *pseudo*-C_{2v} symmetry.
[d] *pseudo*-C_i symmetry.
[e] The excitation wavelength was 350 nm.
[f] The excitation wavelength was 370 nm.
[g] The excitation wavelength was 400 nm.
[h] The excitation wavelength was 430 nm.
[i] The excitation wavelength was 410 nm.
[j] The excitation wavelength was 420 nm.
[k] The excitation wavelength was 440 nm.
[l] The excitation wavelength was 450 nm.

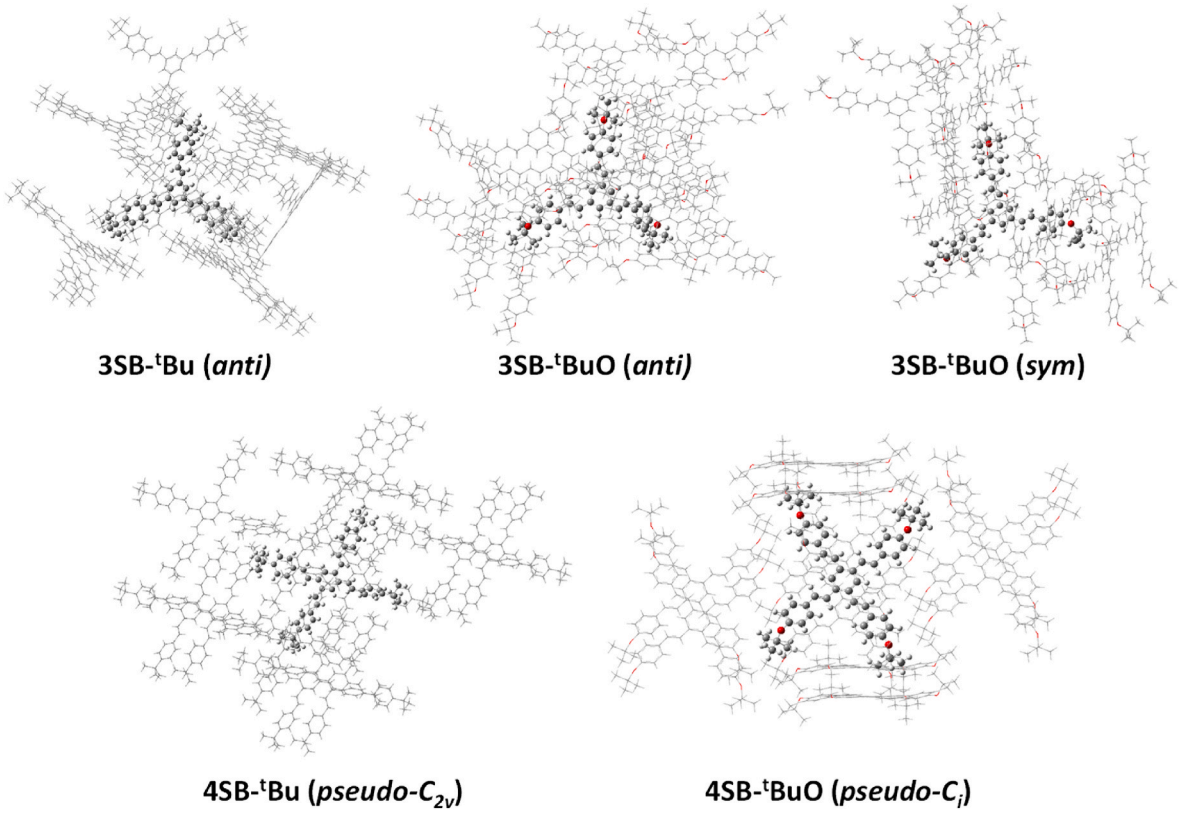

Fig. 5. QM/MM model clusters for the studied compounds. The active molecule is treated as high level (M06-2X/6-31G**) and the surrounding molecules as low level (UFF).

increasing de fluorescence emission in the solid state [59]. Therefore, the existence of columns of *anti*-**3SB-^{t}BuO** molecules with C-H···π intramolecular contacts and absence of π-π interactions could be associated to higher fluorescence quantum yield of **3SB-^{t}BuO** with respect to **3SB-^{t}Bu**. Here, it should be remembered that some twisting normal modes of the styryl moieties are involved in the non-radiative IC decay of *anti*-**3SB-^{t}BuO** in solution. In the solid state, the hindering of these vibrations because of C-H···π intramolecular contacts should reduce the efficiency of the non-radiative deactivation.

In addition, the short-range excitonic effects of **3SB-^{t}Bu** and **3SB-^{t}BuO** were analyzed for those molecular dimers with the highest electronic couplings in the crystal. Thus, in the context of the Spano and Hestand formalism [24,25], the photophysical behavior can be estimated from the sign of the charge-transfer intermolecular coupling, J_{CT} α $-(t_h t_e)$, where t_h and t_e are the hole and electron transfer integrals between neighboring chromophores. Interestingly, the sign of J_{CT} depends on the column selected in the crystal both for **3SB-^{t}Bu** and **3SB-^{t}BuO** (see Table 3). In the case of **3SB-^{t}BuO**, for instance, J_{CT} is negative if the molecular dimer is extracted from the columns of the conformer *sym*-**3SB-^{t}BuO** while J_{CT} turns to be positive for the columns of *anti*-**3SB-^{t}BuO**. In a simplistic treatment it could be expected that *sym*-**3SB-^{t}BuO** columns had J-type behavior (bathochromic spectral shifts) and *anti*-**3SB-^{t}BuO** columns had H-type behavior (hypochromic spectral shifts). In a rigorous treatment, nevertheless, the spectral shifts of the whole crystal depend on the Davydov components which result from the sum of the excitonic couplings in different crystal orientations (this treatment is far beyond the scope of this article) [60,61].

In the case of the tetra(styryl)benzene derivates, columnar packing (along the *b* axis) was only observed for **4SB-^{t}BuO** with weak π-π interactions at 3.3 Å between the central rings (and a slip angle of 33°). As commented, this distance is higher than the distances between the central rings found for the tris(styryl)benzenes (only excepting the similar distance measured for the columnar packing of the molecule type 1 of **4SB-^{t}BuO**) (see Table S8). Hence, the presence of four *tert*-butoxy groups per molecule seems to increase the steric hindrance, separating the tetra(styryl)benzene molecules in the crystal with respect to the tris (styryl)benzene derivates. In the crystal of **4SB-^{t}Bu**, there are two molecules in the asymmetric unit which adopt a bent conformation where the peripheral rings have dihedral angles with the central ones as high as 53° (see Table S7 and Fig. S25). In the packing of **4SB-^{t}Bu**, weak C-H···O hydrogen bonds with the interstitial solvent are present as well as weak π-π interactions between neighbour molecules (see Fig. S30). The weaker supramolecular bonds observed for the crystal of **4SB-^{t}Bu** led to the rapid loss of crystallinity of this structure (see Fig. S32). Interestingly, the quantum yields determined for the crystal of **4SB-^{t}Bu** are higher than for the crystal of **4SB-^{t}BuO** (and for the rest of solid samples).

3.3. Electroluminescent and semiconducting properties

The photophysical properties described for the synthetized compounds have impelled us to develop proof-of-concept light emitting devices by using these compounds as electroluminescent emissive layer. Previously, the semiconducting properties of the active compounds were evaluated to have a broader perspective on their optoelectronic potential. Thus, different parameters related to the charge injection and transport processes were calculated at the B3LYP/6-31G** level of theory. B3LYP is one of the most employed functionals for the study of electronic properties in organic semiconductors and provides reasonable linear relationship between the experimental ionization potential and electron affinity and calculated HOMO and LUMO energy levels, respectively [62–64]. Table 4 shows the adiabatic ionization potential (AIP), adiabatic electron affinity (AEA) as well as hole and electron reorganization energies (λ_h and λ_e) calculated in gas phase. The hole and electron transfer rate constant (k_h and k_e) were estimated using the Marcus' equation (4) for the dominant charge-hopping pathways in the crystal. These charge-hopping pathways correspond to the molecular arrangements in which the hole and electron couplings are maximized (Fig. S41). The value of the reorganization energy and charge transfer integral must be minimized and maximized, respectively, to achieve semiconductor materials with high charge transfer rate constants [65]. Slightly smaller λ_e values were computed for the tris(styryl)benzene derivatives (0.18–0.21 eV) than for the tetra(styryl)benzene derivatives (0.26–0.30 eV). λ_h is sensitive to both the number of branches of the core and the nature of the side chains. This energy is significantly smaller for the tris(styryl)benzenes with *tert*-butyl side chains (0.17 eV for **3SB-^{t}Bu**) than for the tetra(styryl)benzenes with *tert*-butoxy chains (0.67 eV for **4SB-^{t}BuO**).

The highest charge rate constants were calculated for the tris(styryl) benzene derivates because they generally have smaller reorganization energies and higher transfer integrals (Tables 3 and 4). For instance, $k_h \geq 2.6 \times 10^{13}\ s^{-1}$ for **3SB-^{t}Bu** (molecules type 1 and 2) and $k_e \geq 1.1 \times 10^{13}\ s^{-1}$ for both **3SB-^{t}OBu** (molecules type 1 and 2) and **3SB-^{t}Bu** (only molecules type 2). Interestingly, balanced hole and electron transfer rate constants were found for the molecular arrangement type 2 of **3SB-^{t}Bu** ($k_h/k_e = 2.4$) and for **4SB-^{t}Bu** ($k_h/k_e = 3.3$). Thus, exclusively considering the charge transfer rate constants, a better device performance could be expected for single-layer OLEDs based on **3SB-^{t}Bu** and **4SB-^{t}Bu** than those based on their *tert*-butoxy homologues **3SB-^{t}OBu** and **4SB-^{t}OBu**. Unfortunately, the results obtained in the electroluminescent experiments did not totally match with these preliminary predictions (*vide infra*). However, this result should not be surprising because we must also assume that the supramolecular structure of the active layer of the OLED (obtained by spin coating) could be different to the crystal structure (employed for our theoretical calculations). The differences in the molecular packing would have a great impact on the value of charge transfer integral due to it is extremely sensitive to small displacements between neighboring molecules, and as a consequence, on the charge rate constants [17].

In addition, other many factors might have a significant impact on the device performance, as for instance the charge injection efficiency.

Table 3
Electron (t_e) and hole (t_h) couplings calculated at the M06-2X/6-31G** level of theory for dimers extracted from the crystal X-ray structure. The dimers are shown in Fig. S41.

Compound	t_h (meV)	t_e (meV)	$t_h \cdot t_e$ (meV [2])
anti-**3SB-^{t}Bu** (type 1)	83.2	−10.9	−907
anti-**3SB-^{t}Bu** (type 2)	−55.4	−39.0	2161
anti-**3SB-^{t}BuO** (type 1)	−16.3	85.1	−1387
sym-**3SB-^{t}BuO** (type 2)	36.4	53.6	1951
4SB-^{t}Bu (C_{2v})	32.8	35.5	1164
4SB-^{t}BuO (C_i)	14.6	14.9	218

Table 4
Adiabatic ionization potential (AIP), electron affinities (AEA), reorganization energies (λ_h and λ_e) and charge transfer rate constant (k_h and k_e) for hole and electron, respectively, calculated at the B3LYP/6-31G** level of theory in gas phase.

Compound	AIP (eV)	AEA (eV)	λ_h (eV)	λ_e (eV)	k_h (s^{-1})	k_e (s^{-1})
anti-**3SB-^{t}Bu** (type 1)	6.28	0.54	0.165	0.178	5.75×10^{13}	8.37×10^{11}
anti-**3SB-^{t}Bu** (type 2)	6.28	0.54	0.165	0.178	2.55×10^{13}	1.07×10^{13}
anti-**3SB-^{t}BuO** (type 1)	6.09	0.55	0.384	0.208	1.71×10^{11}	3.52×10^{13}
sym-**3SB-^{t}BuO** (type 2)	6.09	0.45	0.402	0.204	7.01×10^{11}	1.47×10^{13}
4SB-^{t}Bu (C_{2v})	5.73	1.01	0.183	0.296	7.12×10^{12}	2.18×10^{12}
4SB-^{t}BuO (C_i)	5.45	0.95	0.668	0.261	6.57×10^{9}	5.75×10^{11}

In this sense, DFT calculations predicted significant higher AEAs and AIPs for the tetra(styryl)benzene derivates than for their tribranched homologues. Higher AEA and AIP values are commonly associated with higher hole and electron injection efficiencies [65]. The HOMO-LUMO energy gap is also smaller for the tetra(styryl)benzenes than for the tris(styryl)benzenes (Fig. 6(a); Tables 4 and S15). Consequently, smaller charge injection barriers from the cathode and anode to the active material are expected for the tetra(styryl)benzenes. Similar conclusions were reported for related oligo(styryl)benzenes with methyl and methoxy side chains [32]. As described below, four single-layer light--emitting devices formed by ITO/PEDOT:PSS/active compound/Al were fabricated using each one of the studied compounds as active layer. Thus, the hole injection barrier to the active material is between 0.6 and 0.9 eV considering a HOMO energy of −5.1 eV for the injection layer [66] and HOMO energies estimated from cyclic voltammetry (CV) for the studied compounds (Fig. 6(a), S21 and S22). As expected, smaller hole injection barriers were calculated for the tetra(styryl)benzenes (0.6–0.7 eV) than for the tris(styryl)benzenes (0.7–0.9 eV). These barriers are even smaller considering the HOMO energies calculated by B3LYP for the studied compounds. On the contrary, higher metal-organic barriers are expected for electron injection and hence it seems to be less efficient than the hole injection. Unfortunately, LUMO energies could not be estimated from CV for the studied compounds but values of −3.39 eV and −3.38 eV were reported for the analogue compounds **3SB-CH$_3$** and **4SB-CH$_3$**, respectively (see Scheme 1) [32]. Considering that these LUMO energies were comparable to those of their *tert*-butyl and *tert*-butoxy derivatives, electron injection barriers of about 0.9 eV with respect to the Al electrode (with a work function of −4.3 eV) would be expected [66]. Although these barriers are even higher take into account the LUMO energy values calculated with B3LYP (2.5–2.9 eV), it was observed that the barriers predicted for the tetra(styryl) benzenes are slightly smaller than for the tris(styryl)benzenes. Based on the described results, a more efficient charge injection (both for holes and electrons) might be expected for **4SB-^{t}Bu** and **4SB-^{t}OBu** than for **3SB-^{t}Bu** and **3SB-^{t}OBu**.

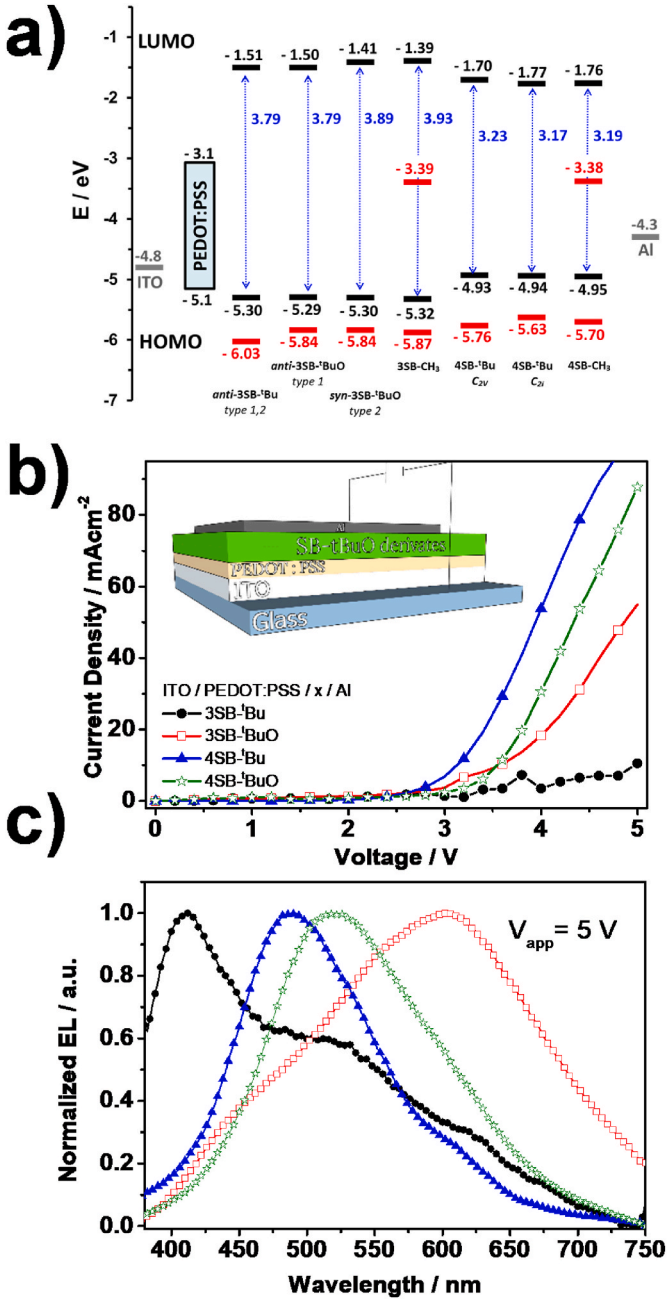

Fig. 6. (a) (Black bars) HOMO and LUMO energy levels (in eV) calculated for the studied compounds (**3SB-^{t}Bu**, **3SB-^{t}BuO**, **4SB-^{t}Bu** and **4SB-^{t}BuO**) at the B3LYP/6-31G** level of theory in gas phase and reported for some related compounds (**3SB-CH$_3$** and **4SB-CH$_3$**) [32]. (Red bars) HOMO energy levels were also estimated from OSWV (Osteryoung square wave voltammetry) oxidation curves, assuming the absolute energy level of ferrocene/ferrocenium to be 5.1 eV below vacuum. (Red bars) The HOMO and LUMO energy levels (estimated from OSWV) reported for **3SB-CH$_3$** and **4SB-CH$_3$** were also included [32]. (b) Current vs voltage curve and (c) electroluminescence spectra of the prepared OLEDs from the selected compounds at 5V. The inset in b) shows a schematic representation of the OLED architecture.

The current-voltage curves of the single-layer devices fabricated using the previously described configuration are shown in Fig. 6(b). These curves exhibit typical diode characteristics [67] with a turn-on voltage ranging from 2.5 to 5.0 V, depending on the emissive layer. The differences observed on the turn-on voltage as well as on the current density can be related to the charge injection efficiency and charge transfer rate constants. Thus, the lowest turn-on voltage was found for **4SB-^{t}Bu** (2.5 eV), following by **4SB-^{t}OBu** (3.0 eV) and **3SB-^{t}OBu** (3.0 eV). Based on the theoretical results, the combination of higher charge injection efficiency and balanced electron-hole mobility theoretically predicted for **4SB-^{t}Bu** would give higher exciton recombination and therefore lower turn on voltages. A higher turn-on voltage (9.0 eV) was reported for a similar device using **3SB-OC$_6$H$_{13}$** in the light-emitting layer [68]. Interestingly, larger differences were found between the EL (electroluminescence) and PL (photoluminescence) emission spectra for the tris(styryl)benzene derivates than for their tetra-branched counterparts (see Fig. 6(c) and Table S4). A green emission band appears at around 550 nm in the EL spectrum of **3SB-^{t}Bu** while the emission maximum does not shift with respect to the PL emission spectrum. A similar behavior was reported for **3SB-OC$_6$H$_{13}$** being the EL band observed at 550 nm attributed to the presence of interfacial traps in the device created during the fabrication process [68]. In the case of **3SB-^{t}OBu**, the differences between EL and PL emission spectra are even more noticeable. A red-shifted band centered at 605 nm appears in the EL emission spectrum. The pristine band centered at 424 nm in the PL spectrum appears in the EL spectrum as a tail of the more intense band at 605 nm. These results can also be related to the effect of the packing on OLED working.

This is not the first time where red-shifted emission bands appears in the EL spectra, and in particular it was quite explored that tris(styryl) benzene derivatives can trap the carriers (electrons-holes) which could be recombined (known as electromers) [69–72]. The possibility of having electromers is not only supported by a significantly broadening of the tris(styryl)benzene derivative crystals over than the tetra(styryl) benzenes (Table S4), also by the highest electronic couplings calculated before (Table 3). It is worth to note that the results indicate better device performance for tetra(styryl)benzene derivatives (higher current density and EL intensity), as electron-hole recombination as electromer is

reduced in favor of the desired EL spectra. Thus, it is not a surprising that **4SB-^{t}Bu** device (the one with the narrowest EL spectrum, and comparable to its PL spectrum; FWHM is 2920 and 3522 cm^{-1}, respectively) yielded the highest current density and EL intensity. On the other hand, the **3SB-^{t}Bu** device mainly gives the EL emission of the electromer, and consequently unmatched EL and PL spectra are obtained. Remarkably, this behavior is agreement with the DFT calculations (vide supra), where more efficient charge injection and balanced hole-electron transport were predicted for the tetra(styryl)benzene derivatives in comparison to the tris(styryl)benzenes. Therefore, beyond the electronic properties of the fluorophore employed in an OLED, the nature, form, and size of its side groups play also a critical role and they should be considered in order to improve the device performance. For instance, some recent works have been reported on related compounds with peripheral bulky groups linked to a benzene core in which AIEE and TADF (thermally activated delayed fluorescence) properties are observed at the same time [73–76]. The incorporation of bulky side groups in the fluorophore does not necessarily lead to a worse semiconductor performance but it can have a significant effect on the supramolecular structure and the electromer formation in the emitting layer.

4. Conclusions

The effect of branched substituents as *tert*-butyl and *tert*-butoxy on the intermolecular interactions, supramolecular structure, photophysical and electroluminescent properties of tris(styryl)benzenes and tetra(styryl)benzenes has been studied. In general, the substitution of *n*-alkyl and *n*-alkoxy side chains by *tert*-butyl and *tert*-butoxy groups does not have a significant impact on absorption and emissive properties in solution of the studied compounds. Nevertheless, *tert*-butyl and *tert*-butoxy side chains seem to have a significant contribution to the normal modes associated with the non-radiative deactivation (IC). AIEE phenomena was observed for all the studied compounds while in the case of their *n*-alkoxy derivatives was only reported for **3SB-OC$_6$H$_{13}$** but not for **4SB-OC$_6$H$_{13}$** [19]. Thus, the normal modes involving *tert*-butyl and *tert*-butoxy groups seem to be more efficiently blocked upon aggregation than non-branched side chains as *n*-hexyloxy (RIV mechanism). The blocking of the trans→cis photoisomerization upon aggregation could also be a key mechanism associated with AIEE, particularly for the tris(styryl)benzene derivatives.

The *tert*-butyl and *tert*-butoxy groups have a determining role in the supramolecular structure of oligo(styryl)benzenes and their photophysical properties in solid state. It was particularly notorious the increase of the fluorescence quantum yield observed for **4SB-^{t}Bu** and **4SB-^{t}OBu** in the solid state, with respect to the reference compound **4SB-OC$_6$H$_{13}$**. In general, larger distances between the central rings and weaker intermolecular interactions were found in the crystals of the tetra(styryl)benzene derivatives with respect to their tribranched homologues.

Single-layer light-emitting devices were fabricated using each one of the studied compounds as active layer. The substitution of a *n*-alkyl chain by *tert*-butyl and *tert*-butoxy groups did not worsen the performance of emitting devices fabricated with tris(styryl)benzene derivates. In fact, the turn-on voltage measured for both **3SB-^{t}Bu** and **3SB-^{t}OBu** was significantly lower than that reported for **3SB-OC$_6$H$_{13}$** [68]. Considering the whole set of studied compounds, we found that the tetra(styryl)benzene derivatives, and particularly **4SB-^{t}Bu**, showed better device performance, with lower turn-on voltage, higher current density and EL intensity than the tris(styryl)benzenes. This was attributed to a higher propensity of tris(styryl)benzenes to form aggregates and electromers in the active layer of the device. DFT calculations and CV measurements also suggested that the charge injection is more efficient in the tetra(styryl)benzene derivatives. Additionally to these findings, the better performance of the emitting device fabricated with **4SB-^{t}Bu** could be also related to a balanced charge transport as predicted by DFT calculations for the crystal structure of this compound. Therefore, the incorporation of *tert*-butyl and *tert*-butoxy side groups in oligo(styryl)benzenes could be a suitable strategy to reduce the electromer formation and improve the performance of light-emitting devices.

CRediT authorship contribution statement

Fernando de Lera-Garrido: carried out the synthesis and spectroscopic measurements. **Rocío Domínguez:** carried out the synthesis and spectroscopic measurements. **M. Paz Fernández-Liencres:** performed DFT calculations. **Cristina Martín:** performed the electroluminescent experiments. **Juan Tolosa:** supervised the synthesis and performed the characterization of all compounds prepared. **Eva M. García-Frutos:** obtained the crystals and solved the X-ray structure of the studied compounds. **Josefina Perles:** obtained the crystals and solved the X-ray structure of the studied compounds, All authors contributed to the results discussions and agreed with the results, All authors contributed to writing the manuscript. **Johan Hofkens:** performed the electroluminescent experiments. **Joaquín C. García-Martínez:** conceived the idea, designed and coordinated the experiments between researchers and wrote the manuscript. **Andrés Garzón-Ruiz:** conceived the idea, designed and coordinated the experiments between researchers and wrote the manuscript. **Amparo Navarro:** conceived the idea, designed and coordinated the experiments between researchers and wrote the manuscript.

Declaration of competing interest

The authors declare the following financial interests/personal relationships which may be considered as potential competing interests:

Joaquin C. Martinez Garcia reports financial support was provided by Ministerio de Economía y Competitividad (Government of Spain) and University of Castilla-La Mancha. Eva M Garcia Frutos reports financial support was provided by Ministerio de Ciencia e Innovación (Government of Spain). Amparo Navarro reports financial support was provided by Consejería de Transformación Económica, Industria, Conocimiento y Universidades (Junta de Andalucía), Universidad de Jaén y Centro de Servicios de Informática y Redes de Comunicaciones' (CSIRC) (Universidad de Granada). Andrés Garzón Ruiz reports equipment, drugs, or supplies was provided by University of Castilla-La Mancha. Andrés Garzón Ruiz reports financial support was provided by Junta de Comunidades de Castilla-La Mancha.

Data availability

Data will be made available on request.

Acknowledgments

The authors would like to thank the Ministerio de Economía y Competitividad (Spain) (project CTQ2017-84561-P), Universidad de Castilla-La Mancha (Grant Nos. 2019-GRIN-27152, 2020-GRIN-28866, 2021-GRIN-30998) and Universidad de Jaén (FEDER_UJA_2020; project 2021/00627/001) for supporting the research described in this article. This work was also supported by the Ministerio de Ciencia e Innovación (Spain) (MCIN/AEI/https://doi.org/10.13039/501100011033, project PID2019-105479RB-I00). The computational study was financially supported by 'Consejería de Transformación Económica, Industria, Conocimiento y Universidades' Junta de Andalucía (FQM-337) and 'Acción 1' (Universidad de Jaén, Spain). The authors thank to 'Centro de Servicios de Informática y Redes de Comunicaciones' (CSIRC) (Universidad de Granada, Spain) for providing the computing time. The authors also thank to Dr. Gustavo de Miguel (University of Cordoba) for his technical support.

Appendix A. Supplementary data

Supplementary data to this article can be found online at https://doi.org/10.1016/j.dyepig.2023.111179.

References

[1] Li Y, Zhang Y, Zuo X, Lin Y. Organic photovoltaic electron acceptors showing aggregation-induced emission for reduced nonradiative recombination. Chem Commun 2021;57:5135–8.
[2] Bernard RS, Sych G, Nasiri S, Bezvikonnyi O, Volyniuk D, Simokaitiene J, Bucinskas A, Gudeika D, Ariffin A, Grazulevicius JV. Triphenylethylene-based emitters exhibiting aggregation induced emission enhancement and balanced bipolar charge transport for blue non-doped organic light-emitting diodes. Synth Met 2021;271:116641.
[3] Zhao E, Chen S. Materials with aggregation-induced emission characteristics for applications in diagnosis, theragnosis, disease mechanism study and personalized medicine. Mater Chem Front 2021;5:3322–43.
[4] Jang SE, Qiu L, Cai X, Wei J, Lee L, Zhang W, Tan EK, Liu B, Zeng L. Aggregation-induced emission (AIE) nanoparticles labeled human embryonic stem cells (hESCs)-derived neurons for transplantation. Biomaterials 2021;271:120747.
[5] Würthner F. Aggregation-induced emission (AIE): a historical perspective. Angew Chem Int Ed 2020;59:14192–6.
[6] Wang G, Yang L, Li C, Yu H, He Z, Yang C, Sun J, Zhang P, Gu X, Tang BZ. Novel strategy to prepare fluorescent polymeric nanoparticles based on aggregation-induced emission via precipitation polymerization for fluorescent lateral flow assay. Mater Chem Front 2021;5:2452–8.
[7] Domínguez R, Navarro A, García-Martínez JC. Styrylbenzene organogels and how the cyano groups tune the aggregation-induced emission geles. Dyes Pigments 2021;192:109427.
[8] de Lera-Garrido F, Sanchez-Ruiz A, Rodríguez-Lopez J, Tolosa J, García-Martínez JC. Enhancement of emission by surfactant-induced aggregation in poly (phenylenevinylene)-based lipochromophores. Dyes Pigments 2020;179:108410.
[9] Li Q, Li Z. The strong light-emission materials in the aggregated state: what happens from a single molecule to the collective group. Adv Sci 2017;4:1600484.
[10] Wang B, Wu Z, Fang B, Yin M. Blue-shifted mechanochromism of a dimethoxynaphthalene-based crystal with aggregation-induced emission. Dyes Pigments 2020;182:108618.
[11] Gierschner J, Shi J, Milián-Medina B, Roca-Sanjuán D, Varghese S, Park SY. Luminescence in crystalline organic materials: from molecules to molecular solids. Adv Opt Mater 2021;9:2002251.
[12] Förster T, Kasper K. Ein konzentrationsumschlag der fluoreszenz. Phys Chem 1954;1:275.
[13] Xiong Y, Yan X, Ma Y, Li Y, Yin G, Chen L. Regulating piezofluorochromism of 9,10-bis(butoxystyryl)anthracenes by isomerization of butyl group. Chem Commun 2015;51:3403–6.
[14] Pan S, Liu K, Ye Y, Gao X, Tang Z, Ye Z, Yu N, Guo K, Wei B. Decrease of intermolecular interactions for less-doped efficient deep blue monomer light-emitting diodes. Org Electron 2020;78:105577.
[15] Zhao Y, Liang WZ. Charge transfer in organic molecules for solar cells: theoretical perspective. Chem Soc Rev 2012;41:1075–87.
[16] Wang L, Nan G, Yang X, Peng Q, Li Q, Shuai Z. Computational methods for design of organic materials with high charge mobility. Chem Soc Rev 2010;39:423–34.
[17] Coropceanu V, Cornil J, da Silva Filho DA, Olivier Y, Silbey R, Brédas JL. Charge transport in organic semiconductors. Chem Rev 2007;107:926–52.
[18] Garzón A, Fernández-Liencres MP, Moral M, Peña-Ruiz T, Navarro A, Tolosa J, Canales-Vazquez J, Hermida-Merino D, Bravo I, Albaladejo J, García-Martínez JC. Effect of the aggregation on the photophysical properties of a blue-emitting star-shaped molecule based on 1,3,5-tristyrylbenzene. J Phys Chem C 2017;121:4720–33.
[19] Domínguez R, Moral M, Fernández-Liencres MP, Peña-Ruiz T, Tolosa J, Canales-Vázquez J, García-Martínez JC, Navarro A, Garzón-Ruiz A. Understanding the driving mechanisms of enhanced luminescence emission of oligo(styryl)benzenes and tri(styryl)-s-triazine. Chem Eur J 2020;26:1–13.
[20] Sánchez-Ruiz A, Rodríguez-López J, Garzón-Ruiz A, Jiménez-Pulido SB, Illán-Cabeza NA, Navarro A, García-Martínez JC. Shedding light on the origin of solid-state luminescence enhancement in butterfly molecules. Chem Eur J 2020;26:13990–4001.
[21] McRae EG, Kasha MJ. Enhancement of phosphorescence ability upon aggregation of dye molecules. J Chem Phys 1958;28:721.
[22] Kasha M. Energy transfer mechanisms and the molecular exciton model for molecular aggregates. Radiat Res 1963;20:55–70.
[23] Kasha M, Rawls HR, Ashraf El-Bayoumi M. The exciton model in molecular spectroscopy. Pure Appl Chem 1965;11:371–92.
[24] Hestand NJ, Spano FC. Molecular aggregate photophysics beyond the Kasha model: novel design principles for organic materials. Acc Chem Res 2017;50:341–50.
[25] Hestand NJ, Spano FC. Expanded theory of H- and J-molecular aggregates: the effects of vibronic coupling and intermolecular charge transfer. Chem Rev 2018;118:7069–163.
[26] Mei J, Leung NLC, Kwok RTK, Lam JWY, Tang BZ. Aggregation-induced emission: together we shine, united we soar. Chem Rev 2015;115:11718–940.
[27] Yamaguchi M, Ito S, Hirose A, Tanaka K, Chujo Y. Control of aggregation-induced emission versus fluorescence aggregation-caused quenching by bond existence at a single site in boron pyridinoiminate complexes. Mater Chem Front 2017;1:1573–9. Y.
[28] Wang H, Zhao E, Lam JWY, Tang BZ. AIE Luminogens: emission brightened by aggregation. Mater Today 2015;18:365–77.
[29] Crespo-Otero R, Li Q, Blancafort L. Chem Asian J 2019;14:700–14.
[30] Padalkar VS, Seki S. Excited-state intramolecular proton-transfer (ESIPT)-inspired solid state emitters. Chem Soc Rev 2016;45:169–202.
[31] Chen Y, Fang Y, Gu H, Qiang J, Li H, Fan J, Cao J, Wang F, Lu S, Chen X. Color-tunable and ESIPT-inspired solid fluorophores based on benzothiazole derivatives: aggregation-induced emission, strong solvatochromic effect, and white light emission. ACS Appl Mater Interfaces 2020;12:55094–106.
[32] Moral M, Domínguez R, Fernández-Liencres MP, Garzón-Ruiz A, García-Martínez JC, Navarro A. Photophysical features and semiconducting properties of propeller-shaped oligo(styryl)benzenes. J Chem Phys 2019;150:064309.
[33] Burroughes HH, Bradley DDC, Brown AR, Marks RN, Mackay K, Fried RH, Burn PL, Holmes AB. Light-emitting diodes based on conjugated polymers. Nature 1990;347:539.
[34] Oelkrug D, Tompert A, Egelhaaf HJ, Hanack M, Steinhuber E, Hohloch M, Meier H, Stalmach U. Towards highly luminescent phenylene vinylene films. Synth Met 1996;83:231–7.
[35] Frisch MJ, et al. Gaussian 09, revision D.01. Wallingford, CT: Gaussian, Inc.; 2009.
[36] Zhao Y, Truhlar DG. The M06 suite of density functionals for main group thermochemistry, thermochemical kinetics, noncovalent interactions, excited states, and transition elements: two new functionals and systematic testing of four M06-class functionals and 12 other functionals. Theor Chem Acc 2008;120:215–41.
[37] Cossi M, Rega N, Scalmani G, Barone V. Energies, structures, and electronic properties of molecules in solution with the C-PCM solvation model. J Comput Chem 2003;24:669–81.
[38] Tomasi J, Mennucci B, Cammi R. Quantum mechanical continuum solvation models. Chem Rev 2005;105:2999–3094.
[39] Cammi R, Corni S, Mennucci B, Tomasi J. Electronic excitation energies of molecules in solution: state specific and linear response methods for nonequilibrium continuum solvation models. J Chem Phys 2005;122:104513.
[40] Improta R, Barone V, Scalmani G, Frisch MJ. A state-specific polarizable continuum model time dependent density functional theory method for excited state calculations in solution. J Chem Phys 2006;125:54103.
[41] Scalmani G, Frisch MJ, Mennucci B, Tomasi J, Cammi R, Barone V. Geometries and properties of excited states in the gas phase and in solution: theory and application of a time-dependent density functional theory polarizable continuum model. J Chem Phys 2006;124:94107.
[42] Reimers JR. A practical method for the use of curvilinear coordinates in calculations of normal-mode-projected displacements and Duschinsky rotation matrices for large molecules. J Chem Phys 2001;115:9103–9109.
[43] Köhler A, Bässler H. Electronic processes in organic semiconductors: an introduction. Weinheim: Wiley-VCH; 2015.
[44] Dapprich S, Komaromi I, Byun KS, Morokuma K, Frisch MJ. A new ONIOM implementation in Gaussian98. Part I. The calculation of energies, gradients, vibrational frequencies and electric field derivatives. J Mol Struct: THEOCHEM 1999;461:1–21.
[45] Vreven T, Morokuma K, Farkas Ö, Schlegel HB, Frisch MJ. Geometry optimization with QM/MM, ONIOM, and other combined methods. I. microiterations and constraints. J Comput Chem 2003;24:760–9.
[46] Lin H, Truhlar D. QM/MM: what have we learned, where are we, and where do we go from here? Theor Chem Acc 2007;117:185–99.
[47] Casewit CJ, Colwell KS, Rappe AK. Application of a universal force field to organic molecules. J Am Chem Soc 1992;114:10035–46.
[48] Marcus RA. Electron transfer reactions in chemistry. Theory and experiment. Rev. Mod. Phys. 1993;65:599–610.
[49] Baumeier B, Kirkpatrick J, Andrienko D. Density-functional based determination of intermolecular charge transfer properties for large-scale morphologies. Phys Chem Chem Phys 2010;12:11103–13.
[50] Kirkpatrick J. An approximate method for calculating transfer integrals based on the ZINDO Hamiltonian. Int J Quant Chem 2007;108:51–6.
[51] Gierschner J, Lüer L, Milián-Medina B, Oelkrug D, Egelhaaf HJ. Highly emissive H-aggregates or aggregation-induced emission quenching? the photophysics of all-trans para-distyrylbenzene. J Phys Chem Lett 2013;4:2686–97.
[52] Gierschner J, Mack HG, Lüer L, Oelkrug D. Fluorescence and absorption spectra of oligophenylenevinylenes: vibronic coupling, band shapes and solvatochromism. J Chem Phys 2002;116:8596.
[53] Shi J, Aguilar Suarez LE, Yoon SJ, Varghese S, Serpa C, Park SY, Leer L, Roca-Sanjuán D, Milián-Medina B, Gierschner J. Solid state luminescence enhancement in π-conjugated materials: unraveling the mechanism beyond the framework of AIE/AIEE. J Phys Chem C 2017;121:23166–83.
[54] Ehlers P, Hakobyan A, Neubauer A, Lochbrunner S, Langer P. Tetraalkynylated and tetraalkenylated benzenes and pyridines: synthesis and photophysical properties. Adv Synth Catal 2013;355:1849–58.
[55] Oelkrug D, Rempfer K, Prass E, Meier H. Fluoreszenz-untersuchungenan distyrylbenzolen. Zeitschrift fer naturforschung A 1988;43:583–90.
[56] Meier H, Zertani R, Noller K, Oelkrug D, Krabichler G. Fluoreszenz-untersuchungen an styrylsubstituierten benzolen. Chem Ber 1986;119:1716–24.
[57] Li D, Wang J, Ma X. White-light-emitting materials constructed from supramolecular approaches. Adv Opt Mater 2018;6:1800273.
[58] Xie Z, Yu T, Chen J, Ubba E, Wang L, Mao Z, Su T, Zhang Y, Aldred MP, Chi Z. Weak interactions but potent effect: tunable mechanoluminescence by adjusting intermolecular C–H···π Interactions. Chem Sci 2018;9:5787–94.

[59] Yu B, Liu D, Wang Y, Zhang T, Zhang YM, Li M, Zhang SXA. Strong and insusceptible photo-emissions from an intramolecular weak hydrogen bond strengthened twisted fluorophore. Phys Chem Chem Phys 2018;20:23851–5.
[60] Davydov AS. Theory of molecular excitons. first ed. Springer; 1971.
[61] Schwoerer M, Wolf HC. Organic molecular solid. Wiley-VCH; 2006.
[62] Zhan CG, Nichols JA, Dixon DA. Ionization potential, electron affinity, electronegativity, hardness, and electron excitation energy: molecular properties from density functional theory orbital energies. J Phys Chem A 2003;107:4184–95.
[63] Rienstra-Kiracofe JC, Tschumper GS, Schaefer III HF, Nandi S, Ellison GB. Atomic and molecular electron affinities: photoelectron experiments and theoretical computations. Chem Rev 2002;102:231–82.
[64] Muscat J, Wander A, Harrison NM. On the prediction of band gaps from hybrid functional theory. Chem Phys Lett 2001;342:397–401.
[65] Newman CR, Frisbie CD, da Silva Filho DA, Brédas JL, Ewbank PC, Mann KR. Introduction to organic thin film transistors and design of n-channel organic semiconductors. Chem Mater 2004;16:4436–51.
[66] Martín C, Kennes K, Van der Auweraer M, Hofkens J, de Miguel G, García-Frutos EM. Self-assembling azaindole organogel for organic light-emitting devices (OLEDs). Adv Funct Mater 2017;27:1702176.
[67] Sah CT, Noyce RN, Shockley W. Carrier generation and recombination in P-N junctions and P-N junction characteristics. Proceedings of the IRE 1957;45:1228–43.
[68] Coya C, de Andrés A, Zaldo C, Álvarez AL, Arredondo B, Gómez R, Segura JL, Seoane C. Full-solution-processed blue organic light emitting device based on a fluorescent 1,3,5-tristyrylbenzene stilbenoid small molecule. J Appl Phys 2009;105:044510.
[69] Kalinowski J, Giro G, Cocchi M, Fattori V, Di Marco P. Unusual disparity in electroluminescence and photoluminescence spectra of vacuum-evaporated films of 1,1-bis((di-4-tolylamino)phenyl)cyclohexane. Appl Phys Lett 2000;76:2352.
[70] Farinola GM, Ragni R. Electroluminescent materials for white organic light emitting diodes. Chem Soc Rev 2011;40:3467–82.
[71] Sarkar SK, Kumar GR, Thilagar P. White light emissive molecular siblings. Chem Commun 2016;52:4175–8.
[72] Martín C, Borreguero C, Kennes K, Van der Auweraer M, Hofkens J, de Miguel G, García-Frutos EM. Bipolar luminescent azaindole derivative exhibiting aggregation-induced emission for non-doped organic light-emitting diodes. J Mater Chem C 2019;7:1222–7.
[73] Mahmoudi M, Gudeika D, Kutsiy S, Simokaitiene J, Butkute R, Skhirtladze L, Woon KL, Volyniuk D, Grazulevicius JV. Ornamenting of blue thermally activated delayed fluorescence emitters by anchor groups for the minimization of solid-state solvation and conformation disorder corollaries in non-doped and doped organic light-emitting diodes. ACS Appl Mater Interfaces 2022;14:40158–72.
[74] Skhirtladze L, Lietonas K, Bucinskas A, Volyniuk D, Mahmoudi M, Mukbaniani O, Woon KL, Ariffin A, Grazulevicius JV. 1,4-Bis(trifluoromethyl)benzene as a new acceptor for the design and synthesis of emitters exhibiting efficient thermally activated delayed fluorescence and electroluminescence: experimental and computational guidance. J Mater Chem C 2022;10:4929–40.
[75] Skuodis E, Bezvikonnyi O, Tomkeviciene A, Volyniuk D, Mimaite V, Lazauskas A, Bucinskas A, Keruckiene R, Sini G, Grazulevicius JV. Aggregation, thermal annealing, and hosting effects on performances of an acridan-based TADF emitter. Org Electron 2018;63:29–40.
[76] Grybauskaite-Kaminskiene G, Volyniuk D, Mimaite V, Bezvikonnyi O, Bucinskas A, Bagdziunas G, Grazulevicius JV. Aggregation-enhanced emission and thermally activated delayed fluorescence of derivatives of 9-phenyl-9H-carbazole: effects of methoxy and tert-butyl Substituents. Chem Eur J 2018;24:9581–91.